Dark Matter Searches on a Photonic Chip

Nikita Blinov,[1,2] Christina Gao,[3,4] Roni Harnik,[4] Ryan Janish,[4] and Neil Sinclair[5]

[1] *Department of Physics and Astronomy, University of Victoria, Victoria, BC V8P 5C2, Canada*
[2] *Department of Physics and Astronomy, York University, Toronto, Ontario, M3J 1P3, Canada*
[3] *Department of Physics, University of Illinois at Urbana-Champaign, Urbana, IL 61801, USA*
[4] *Theoretical Physics Division, Fermi National Accelerator Laboratory, Batavia, IL 60510, USA*
[5] *John A. Paulson School of Engineering and Applied Sciences, Harvard University, 29 Oxford St., Cambridge, MA 02138, USA*

(Dated: January 31, 2024)

Dark matter (DM) with masses of order an electronvolt or below can have a non-zero coupling to electromagnetism. In these models, the ambient DM behaves as a new classical source in Maxwell's equations, which can excite potentially detectable electromagnetic (EM) fields in the laboratory. We describe a new proposal for using integrated photonics to search for such DM candidates with masses in the 0.1 eV - few eV range. This approach offers a wide range of wavelength-scale devices like resonators and waveguides that can enable a novel and exciting experimental program. In particular, we show how refractive index-modulated resonators, such as grooved or periodically-poled microrings, or patterned slabs, support EM modes with efficient coupling to DM. When excited by the DM, these modes can be read out by coupling the resonators to a waveguide that terminates on a micron-scale-sized single photon detector, such as a single pixel of an ultra-quiet charge-coupled device or a superconducting nanowire. We then estimate the sensitivity of this experimental concept in the context of axion-like particle and dark photon models of DM, showing that the scaling and confinement advantages of nanophotonics may enable exploration of new DM parameter space.

I. INTRODUCTION

A multitude of observations of dark matter (DM) across many scales in the universe strongly motivates the existence of particles beyond those contained in the Standard Model (SM) of particle physics [1]. New ultralight bosonic fields, such as axions [2–5], axion-like particles (ALPs) [6] and dark photons (DPs) [5, 7, 8] are particularly attractive candidates for DM. This is because they can be directly connected to ultraviolet completions of the SM such as string theory, or they can explain important issues within the SM, such as the apparent fine-tuning of the neutron electric dipole moment, known as the strong CP problem. Discovering these particles would therefore yield unprecedented insights both into the cosmology of our universe and fundamental physics.

Because of their non-relativistic nature and sub-electronvolt mass, axions, ALPs and dark photons in our galactic neighbourhood can be conveniently described by matter waves with a macroscopic de Broglie wavelength and a frequency set by their mass; as a result, they are often called wave-like DM. In most cases, the rich physics of these models can be encapsulated by a single quantity $\boldsymbol{J}_{\rm DM}$, an effective classical electromagnetic current density, which depends on the local DM density and interaction strength. This is a photon source filling all of space, and because the DM is non-relativistic it is monochromatic, highly uniform, and coherent. Detecting these DM candidates amounts to monitoring any electromagnetic system that would couple to such a background current density. This poses an experimental challenge that is very different from traditional particle physics experiments that search for individual recoils of DM off atoms in ultra-quiet detectors [9, 10].

A classic wave-like DM direct detection technique is the haloscope experiment [11], originally designed to search for axions. In this class of experiments, the DM current density $\boldsymbol{J}_{\rm DM}$ resonantly excites a high-quality cavity mode if the mode frequency is tuned to match that of the DM wave, i.e., the DM mass. A high quality cavity enables the build up of the signal field over the coherence time of the cavity and/or the DM. A similar conversion is possible for dark photon DM.

There is an intense effort to explore DM masses around the 1-10 μeV range, corresponding to frequencies of order a GHz. Cavities with these resonant frequencies are room-sized, enabling a large exposure to the surrounding DM over reasonable time-scales. The Axion Dark Matter eXperiment (ADMX) [12] is the standard bearer in this regime. New developments in quantum sensing (such as squeezing [13], quantum sensor networks [14], or photon counting [15]), as well as advances in cavity technology [16–18] are proving instrumental in hastening and extending the search, particularly to higher masses.

The allowed mass range for axion or dark photon DM, however is significantly broader than the GHz regime [19]. This strongly motivates the study of detection techniques complementary to traditional high-quality radio-frequency cavity-based searches. In particular, if one tried to straightforwardly translate this technique to much lower or higher DM masses, the cavity size quickly becomes too large or too small to be experimentally viable. New developments like lumped element experiments [20, 21], SRF cavities [22, 23], optical reflectors [24], dielectric stacks [25–28] and other metamaterials [29, 30] extend experimental sensitivity across

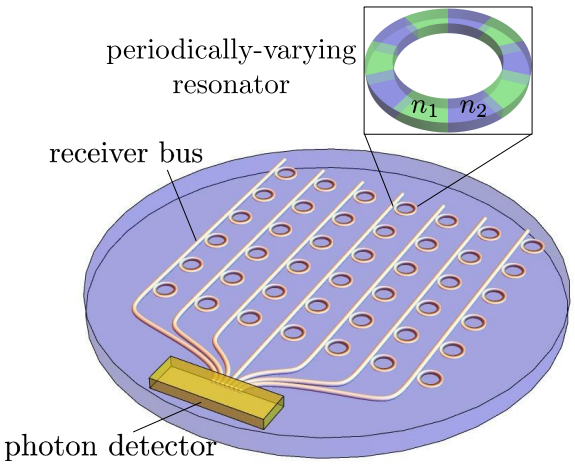

FIG. 1: A schematic setup of an integrated/on-chip photonic system for eV dark matter direct detection. An array of periodically structured resonators are coupled to bus waveguides that run into a photon detector. For axion detection, a background magnetic is also required. The zoom-in shows an example of a resonator: a microring with periodic variations in its index of refraction, which can be attained via, e.g., grooving or periodic poling.

an exponentially large region of light dark matter parameter space.

In this work we propose to use integrated, on-chip, photonic systems to detect eV-range bosonic DM particles. Figure 1 shows a schematic setup, where DM is converted to (signal) light in periodically structured optical resonators which are designed to match the dispersion relations of DM particles and photons. The signal photons are then guided onto micron-sized detectors, such as the Skipper charge-coupled devices (CCDs) [31] or superconducting nanowire single photon detectors (SNSPDs) [32]. Modern lithography techniques allow the fabrication and multiplexing of a large number of compact resonators and waveguides, and enables their assembly into an integrated system. The challenge here is twofold: to ensure a sizable conversion between the non-relativistic DM to photons, and to scan a reasonable DM parameter space. The former can be achieved by refractive index-modulated 1D or 2D photonic structures, whereas the latter can be aided by coupling many resonators to a single receiver bus/waveguide.

We first review how light bosonic DM modifies Maxwell's equations in Section II. We then describe how periodic photonic resonators help convert the DM to photons, and highlight examples of 1D and 2D photonic structures that accomplish this in Section III. An experiment seeking to surpass existing constraints must necessarily use many such resonators, so in Sections IV and V we discuss different strategies for combining and reading out signal photons from large systems of resonators. We then apply these insights to a concrete model consisting of N resonators in series coupled to a single receiver bus and determine the system's response to the DM source in Section VI. Finally, we estimate the sensitivity of these proposed experiments to DM in Section VII. We find that there are strong prospects for detection of DM. Throughout this work we use particle physics ("natural") units, i.e., $\hbar = c = \varepsilon_0 = \mu_0 = 1$.

II. AXION AND DARK PHOTON ELECTRODYNAMICS

Axion or dark photon particles that couple to photons modify classical electrodynamics. When these particles are the dark matter of the universe, they provide a source for the (in-medium) Maxwell equations:

$$\nabla \cdot \boldsymbol{D} \approx 0 \tag{1a}$$
$$\nabla \times \boldsymbol{H} - \partial_t \boldsymbol{D} \approx \boldsymbol{J}_{\rm DM} \tag{1b}$$
$$\nabla \cdot \boldsymbol{B} = 0 \tag{1c}$$
$$\nabla \times \boldsymbol{E} + \partial_t \boldsymbol{B} = 0 \tag{1d}$$

where $\boldsymbol{J}_{\rm DM}$ is the effective DM current density source. In the axion and dark photon models we have

$$\boldsymbol{J}_{\rm DM} = \begin{cases} g_{a\gamma} \boldsymbol{B} \dot{a}(t, \boldsymbol{r}) & \text{axion} \\ \chi m_{A'}^2 \boldsymbol{A'}(t, \boldsymbol{r}) & \text{dark photon} \end{cases} \tag{2}$$

where a and $\boldsymbol{A'}$ stand for the axion (scalar) and the dark photon (vector) field whose amplitudes depend on the local DM density; $g_{a\gamma}$ and χ are coupling parameters encoding the strength of the DM-photon interaction. For DM masses less than ~ 10 eV, the number of DM particles per de Broglie volume is large and so the local DM can be described by a classical Gaussian random field[1]

$$a(\boldsymbol{x}, t) = \int \frac{d^3 v}{(2\pi)^3} \left[\hat{a}(\boldsymbol{v}) e^{-i(\omega t - m \boldsymbol{v} \cdot \boldsymbol{x})} + \text{c.c.} \right], \tag{3}$$

where $\omega \approx m(1 + v^2/2)$; there is an analogous representation of the dark photon field which also includes a sum over its polarizations $\hat{\sigma}_{\mathbf{A}'}$. In Appendix A we show that in the classical regime the two-point correlation function is determined by the local DM density $\rho_{\rm D} \simeq 0.4$ GeV/cm^3 [34] and velocity distribution $f(\boldsymbol{v})$

$$\langle \hat{a}(\boldsymbol{v}) \hat{a}(\boldsymbol{v}')^* \rangle = \frac{\rho_{\rm D}}{2 m_{\rm DM}^2} (2\pi)^6 f(\boldsymbol{v}) \delta^3(\boldsymbol{v} - \boldsymbol{v}'). \tag{4}$$

The typical size of $v \sim 10^{-3}$ is determined by the Galactic virial velocity [35], so the DM is very non-relativistic. This has two important consequences. First,

[1] There is an equivalent representation of the DM fields in terms of a discrete superposition of plane waves [33].

the DM source oscillates at a frequency nearly equal to the DM mass with a coherence time $t_{\rm coh} \sim 2/(m_{\rm DM} v^2) = \text{ns}\,(\text{eV}/m_{\rm DM})$. Second, spatial gradients of the DM field can be neglected on length scales smaller than the DM coherence (de Broglie) length $\lambda_{\rm dB} = 2/(m_{\rm DM} v) = 0.4\ \text{mm}\ (\text{eV}/m_{\rm DM})$.

The DM current density $\boldsymbol{J}_{\rm DM}$ can excite a signal electromagnetic field in any system that supports modes with frequencies and spatial profiles well-matched to DM properties. Below we will make these conditions precise and explore them in optical photonic systems. Because the DM source is approximately monoenergetic (to one part in $1/v^2 \sim 10^6$), typically only a single mode is excited. Taking this signal mode to be of the form $\boldsymbol{E}(\boldsymbol{x})e^{i\omega_R t}$ with $\omega_R \approx m_{\rm D}$ (i.e., the mode is on-resonance with the DM source), the average power[2] that can be collected from this mode is

$$P_{\rm sig} = \frac{Q}{m} \bar{J}^2_{\rm DM} |\eta|^2 V \tag{5}$$

and where we assumed critical coupling (i.e., internal and read-out losses are equal - see Appendix A). Here $\bar{J}^2_{\rm DM}$ parametrises the strength of the DM current $\boldsymbol{J}_{\rm DM}$[3]

$$\bar{J}^2_{\rm DM} = \frac{\rho}{2m^2} \begin{cases} g^2_{a\gamma} m^2 B^2 & \text{axion} \\ \chi^2 m^4/3 & \text{dark photon} \end{cases} . \tag{6}$$

The detailed properties of the detector are encoded by V, its volume; Q, the total/loaded quality factor of the signal mode (here assumed to be smaller than 10^6, the effective DM quality factor) and η, the dimensionless overlap factor[4]

$$|\eta|^2 \equiv \frac{\int d^3x d^3x' \boldsymbol{E}^*(\boldsymbol{x}) \cdot \hat{\boldsymbol{n}} \boldsymbol{E}(\boldsymbol{x}') \cdot \hat{\boldsymbol{n}} e^{-(\boldsymbol{x}-\boldsymbol{x}')^2/\lambda^2_{\rm dB}}}{V \int d\mathbf{x}\ \varepsilon(\boldsymbol{x}) |\boldsymbol{E}|^2} , \tag{7}$$

where $\hat{\boldsymbol{n}}$ represents the direction of external B field for axion DM, or the dark photon polarization $\boldsymbol{\sigma}_{A'}$.

The overlap factor captures two important physical effects. First, it encodes momentum conservation in the underlying DM-to-photon conversion; in free space $|\eta|^2$ vanishes since it is impossible to convert a non-relativistic DM particle with dispersion $\omega \approx m$ (vanishing momentum) to a real photon with dispersion $\omega = k$ because of the momentum mismatch. This necessitates the existence of a detector to "absorb" this mismatch. For example, if the resonator size is comparable to the signal photon wavelength (as for most GHz cavity haloscope experiments), $|\eta|$ can be as big as $\mathcal{O}(1)$. In contrast, at optical frequencies, the resonator size is often much larger than the signal photon wavelength, approximating the free-space limit. In this case, photon momentum along one or more directions is almost conserved. In order for $|\eta|^2$ (and the DM to photon conversion rate) to remain large, photonic structures must break translation invariance on length scales of $\mathcal{O}(1/m)$. As we show below, *periodic* photonic structures fulfill this requirement.

The second important effect encoded in the overlap factor, Eq. (7), is the interference of the signal field produced in different parts of the detector, labelled by $\boldsymbol{x}$ and $\boldsymbol{x}'$. The field from detector elements within a single DM coherence length, i.e., with $|\boldsymbol{x} - \boldsymbol{x}'|/\lambda_{\rm dB} \lesssim 1$ add constructively. On the other hand, $|\eta|^2$ is suppressed if the detector is much larger than a DM coherence length in any direction, as a result the effective detector volume $|\eta|^2 V$, is reduced. This destructive interference arises because the DM source has a different phase in different parts of the detector. As we discuss below, extensive scaling of the total signal power is restored if the detector is able to sum over different signal modes. For most of this paper we will assume that each optical resonator is much smaller than $\lambda_{\rm dB}$ in linear size, but different resonators (whose output can be combined) can be spaced by more than $\lambda_{\rm dB}$.

III. PERIODIC PHOTONIC STRUCTURES

Periodic photonic structures, often referred to as photonic crystals, are designed to control the flow of light in a manner analogous to how semiconductors manipulate the flow of electrons. Periodic photonic structures are characterized by their unique, regularly spaced arrangements of dielectric materials, which create a photonic bandgap – a range of frequencies where light cannot propagate. This control over the behavior of photons has given rise to a wide array of applications, from enhancing the efficiency of lasers and light-emitting diodes to enabling novel, compact optical devices, such as waveguides and filters. In this work we consider optical resonators made from simple periodic structures, such as 1D periodically grooved waveguide [36], and 2D photonic crystal slab [37].

We now specialize to detectors made of periodic photonic structures. The expression for the signal power, Eq. (5), still holds, as the signal field can be expanded in solutions of the source-free Maxwell equations. In an idealized periodic structure of any dimension, however, the overlap factor for the whole dielectric structure can be expressed as a sum over each unit cell. The discrete translation invariance of the dielectric dictates that modes of the source-free version of Eq. (1), i.e., without axion or dark photon DM, take the Bloch form:

$$\boldsymbol{E}_{\boldsymbol{K}} = \boldsymbol{u}_{\boldsymbol{K}}(\boldsymbol{r}) e^{\pm i \boldsymbol{K}\cdot\boldsymbol{r}} , \quad \boldsymbol{u}_{\boldsymbol{K}}(\boldsymbol{r}) = \boldsymbol{u}_{\boldsymbol{K}}(\boldsymbol{r} + \boldsymbol{R}) \tag{8}$$

where $\boldsymbol{K}(\omega)$ is the Bloch wavevector (in the first Brillouin zone) and $\boldsymbol{R}$ is any lattice vector. Solving the source-free Maxwell equations fixes the dispersion relation $\omega =$

[2] Here average refers to the ensemble average over the random DM field, or equivalently, a time average of the power over many coherence times.

[3] For the dark photon this quantity includes an average over polarizations.

[4] Below we took a Gaussian velocity distribution for the DM for simplicity.

$\omega(\boldsymbol{K})$. The denominator of Eq. (7) is then

$$\int d^3r\varepsilon(\boldsymbol{r})|\boldsymbol{E}_{\boldsymbol{K}}|^2 = N_u \int_u d^3r\varepsilon(\boldsymbol{r})|\boldsymbol{u}_{\boldsymbol{K}}(\boldsymbol{r})|^2 \tag{9}$$

where we made use of periodicity of both the dielectric constant and the Bloch function $\boldsymbol{u}_{\boldsymbol{K}}$; N_u is the total number of unit cells in the device and $\int_u$ represents integration over a single unit cell. Similarly, the numerator can be written as

$$\int d^3r\boldsymbol{E}_{\boldsymbol{K}}{}^* \cdot \hat{\boldsymbol{n}} \approx \int_u d^3r e^{-i\boldsymbol{K}\cdot\boldsymbol{r}} u_{\boldsymbol{K}}(\boldsymbol{r}) \sum_i e^{-i\boldsymbol{K}\cdot\boldsymbol{R}_i} \tag{10}$$

where $\boldsymbol{R}_i$ are the positions of each unit cell i and the DM field is assumed to be coherent over the entire resonator (i.e., $\lambda_{\rm dB} \gg$ resonator size). Defining the overlap of a single unit cell as

$$\eta_u = \frac{\frac{1}{V_u}\int_u d^3r e^{-i\boldsymbol{K}\cdot\boldsymbol{r}} u_{\boldsymbol{K}}(\boldsymbol{r})}{\sqrt{\frac{1}{V_u}\int_u d^3r\varepsilon(\boldsymbol{r})|\boldsymbol{u}_{\boldsymbol{K}}(\boldsymbol{r})|^2}}\ , \tag{11}$$

we can write the full overlap factor appearing in the time-averaged signal power as

$$|\eta|^2 = |\eta_u|^2 \frac{1}{N_u^2} \sum_{i,j} e^{-i\boldsymbol{K}\cdot(\boldsymbol{R}_i - \boldsymbol{R}_j)}\ . \tag{12}$$

The detailed form of overlap factor depends on the design of the resonator, which we discuss below. The normalization factor of $1/N_u^2$ is chosen to factor out the volume scaling in Eq. (5). It is important to re-iterate that this expression is valid when the DM is coherent over the entire resonator; this assumption will hold in Section III A, in which we discuss ring resonators. In Section III B we will consider photonic slab resonators which can be larger than a coherence length and Eq. (12) will need to be generalized to include the effects of a non-trivial DM velocity distribution.

A. 1D-Periodic Resonators

First consider a structure that is periodic along a single direction, $\hat{\boldsymbol{z}}$, i.e. $\varepsilon(x,y,z) = \varepsilon(x,y,z+\Lambda)$, where Λ is the length of the unit cell. Assuming that the DM is coherent over the entire structure (i.e., we can neglect variations in DM field over the device) the overlap factor, Eq. (12), simplifies to

$$|\eta|^2 = |\eta_u p_{N_u}(K\Lambda)|^2,\ p_{N_u}(\theta) \equiv \frac{1-e^{-iN_u\theta}}{N_u(1-e^{-i\theta})}, \tag{13}$$

where η_u is the overlap factor for a single unit cell. In the limit of $N_u \gg 1$, $|p_N(K\Lambda)|^2$ is *primarily* peaked at $K=0$ as expected from approximate momentum conservation.

One type of 1D-periodic resonator is a microring (see the insert in Fig. 1), which we can form from N_u unit cells by enforcing an additional periodicity condition $\varepsilon(x,y,z) = \varepsilon(x,y,z+L)$ where the ring circumference is $L = N_u\Lambda$. The field modes in Eq. (8) must be similarly periodic, which selects a discrete subset $K = 2\pi n/L$ for integer n which can be resonantly enhanced. The DM-coupled $K=0$ modes automatically satisfy this condition.

A non-zero DM signal requires $\eta_u \neq 0$. Below we show that this is indeed possible in a 1D-periodic dielectric waveguide with transverse confinement.[5] An analytic treatment is possible only for highly-symmetric geometries so we study a cylindrical periodically-varying waveguide. Other geometries and resonator form-factors generally must be investigated numerically.

Cylindrical Fibre Bragg Grating

By introducing large permittivity modulations periodically along the propagation direction, one can achieve perfect confinement of light even in the presence of radiating modes in the free space (see, e.g., Refs. [38–42]). For simplicity, we consider a step index circular waveguide consisting of a core of radius R and a periodic $\varepsilon(z)$ with periodicity Λ. The cladding has a constant refractive index n_o and a radius much bigger than R. This configuration is also known as a fibre Bragg grating. To accurately describe the leaky fiber modes, below we employ the Fourier modal method [43], which handles the radiating fields analytically. Using the cylindrical coordinates (r,z,ϕ), let $\mathbf{E} \sim (E_r, E_z, E_\phi)e^{im\phi - i\omega t}$, $\mathbf{H} \sim (H_r, H_z, H_\phi)e^{im\phi - i\omega t}$, where m is an integer representing the angular momentum in the plane. The $z-$components of the wave equations are given by

$$\hat{L}_m \begin{pmatrix} E_z \\ H_z \end{pmatrix} = \begin{pmatrix} -(\partial_z \frac{\varepsilon'}{\varepsilon} + \frac{\varepsilon'}{\varepsilon}\partial_z + \omega^2\varepsilon)E_z \\ -\omega^2\varepsilon H_z \end{pmatrix} \tag{14}$$

where $\hat{L}_m \equiv (\frac{1}{r}\partial_r r\partial_r - \frac{m^2}{r^2} + \partial_z^2)$. The solutions take the following form:

$$\begin{pmatrix} \sqrt{\varepsilon}E_z \\ H_z \end{pmatrix} = e^{iKz} \sum_n e^{i2n\pi z/\Lambda} \begin{pmatrix} \psi_n^+(r) \\ \psi_n^-(r) \end{pmatrix} \tag{15}$$

where $+(-)$ represents TM (TE) modes, and n are integers. It can be shown that

$$\psi_n^{\sigma\in\{+,-\}} \sim \begin{cases} \sum_l P_{nl}^\sigma J_m(\lambda_l^\sigma r), & r<R \\ H_m^{(1)}(\alpha_n r), & r>R \end{cases} \tag{16}$$

where J_m and $H_m^{(1)}$ are Bessel functions and Hankel functions of the first kind, and

$$\alpha_n = \sqrt{\omega^2 n_o^2 - (K + 2n\pi/\Lambda)^2}\ . \tag{17}$$

[5] The case without transverse mode confinement corresponds to the wide-area dielectric stack studied in [26].

For confined modes, α_n needs to be imaginary. Thus, when $K = 0$, the $H_m^{(1)}(\alpha_0 r)$ mode is necessarily leaky. The periodic $\varepsilon(z)$ mixes different radial modes via the mixing matrix P_{nl}. More details of ψ_n^σ can be found in Appendix D.

The ϕ components of the fields can be inferred from the $z-$components and will take the following form:

$$\begin{pmatrix} \frac{H_\phi}{\sqrt{\varepsilon}} \\ E_\phi \end{pmatrix} = e^{iKz} \sum_n e^{i2n\pi z/\Lambda} \begin{pmatrix} \chi_n^+(r) \\ \chi_n^-(r) \end{pmatrix}, \tag{18}$$

where $\chi_n^\pm$ are related to $\psi_n^\pm$ by Maxwell's equations. The solutions are obtained by demanding the continuity of E_z, E_ϕ, H_z, H_ϕ at $r = R$. After solving the system, E_r can be obtained via

$$E_r = \frac{-m}{\varepsilon\omega r} H_z + \frac{i}{\omega\varepsilon} \partial_z H_\phi \ . \tag{19}$$

For an arbitrary R, ω is generally complex which determines the intrinsic quality factor of the mode:

$$Q = -\frac{\mathrm{Re}\,\omega}{2\,\mathrm{Im}\,\omega}. \tag{20}$$

One can fine tune the radius of the core R_0 to find a corresponding real solution ω_0, which will be completely confined without considering the additional loss due to bending or surface roughness.

For axion dark matter searches, an external magnetic field will be imposed. If the magnetic field points in the transverse direction of the Bragg grated fibre, say $y-$direction, the modes of interest must break rotational symmetry, i.e. $m > 0$, which will be a hybrid mode of TE and TM polarization. Consider the case of $m = 1, K = 0$. We can estimate η_u by considering the integral $V^{-1}\int_V E_y$ which in terms of cylindrical coordinates is given by

$$\int_0^{2\pi} \frac{d\phi}{2\pi} \int_0^{\Lambda} \frac{dz}{\Lambda} \int_0^{R^2} \frac{dr^2}{R^2} e^{i\phi} \left(E_r \sin\phi + E_\phi \cos\phi\right) \ . \tag{21}$$

Given the form of E_ϕ, integrating over z will pick out the $n = 0$ mode. However, $n = 0$ mode is generally leaky and thus should be highly suppressed for a high Q solution. Similarly, the form of E_r implies that the $\frac{i}{\omega\varepsilon}\partial_z H_\phi$ part should dominantly contribute to the overlap integral, which becomes

$$\frac{1}{V}\int_V E_y \approx \frac{1}{2}\int_0^{\Lambda} \frac{dz}{\Lambda} \int \frac{dr^2}{R^2} \frac{\partial_z \varepsilon^{-1}}{\omega} H_\phi \ . \tag{22}$$

For dark photon dark matter searches, $m = 1, K = 0$ mode would overlap with a transverse dark photon field, whereas $m = 0, K = 0$ mode would overlap with a longitudinal dark photon field. For the latter, η_u is determined by $V^{-1}\int_V E_z$.

Therefore, both the axion and dark photon dark matter dominantly couple to the TM polarization of the zero-K modes. As an example, consider

$$\varepsilon(z) = \begin{cases} \varepsilon_1, & 0 < z < a \\ \varepsilon_2, & a < z < \Lambda \end{cases} \ . \tag{23}$$

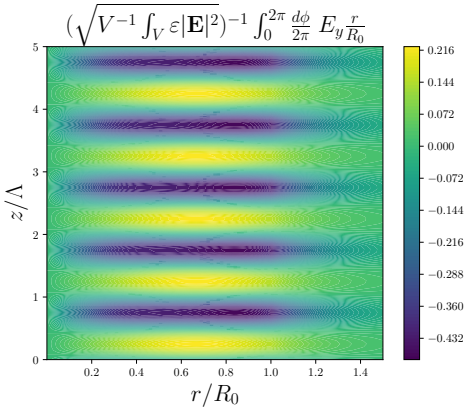

FIG. 2: Normalized profile of $E_y(r,z)\times r$ for a fine-tuned $m = 1, K = 0$ confined mode in a cylindrical fiber Bragg grating. This mode has a non-zero overlap factor η and therefore couples to the DM source. We took a a periodic relative permittivity $\varepsilon = \frac{1}{2}(\varepsilon_1 - \varepsilon_2)\left[1 + \sin(2\pi z/\Lambda)\right] + \varepsilon_2$ with $\varepsilon_2 = 1, \varepsilon_1 = 5$ in the core and $n_o = 1$ in the cladding.

This yields an overlap factor which is approximately

$$\eta_u \sim \begin{cases} \sqrt{2}\frac{(\varepsilon_1 - \varepsilon_2)}{(\varepsilon_1+\varepsilon_2)^{3/2}}, & m = 1 \\ \frac{\varepsilon_1^{1/2} - \varepsilon_2^{1/2}}{\sqrt{2\pi\varepsilon_1\varepsilon_2}} \sin\left(\frac{2a\pi}{\Lambda}\right), & m = 0 \end{cases} \tag{24}$$

where we assume that integrating the radial part yields a factor $\lesssim 1$.

To numerically verify this, we consider a toy example with a periodic permittivity in the core given by $\frac{1}{2}(\varepsilon_1 - \varepsilon_2)\left[1 + \sin(2\pi z/\Lambda)\right] + \varepsilon_2$ with $\varepsilon_2 = 1, \varepsilon_1 = 5$, and $n_o = 1$ in the cladding. We work in the basis of $n = 0, \pm 1$ modes only, and fine tune the radius to obtain a confined mode with $m = 1, K = 0$, which has $\tilde{\omega}_0 \equiv \omega_0/(2\pi/\Lambda) = 0.649038, R_0 = 0.942518/(2\pi/\Lambda)$ (c.f. Figure 2). Up to an overall normalization, the solutions are given by

$$\sqrt{\varepsilon}E_z = 2i\cos\left(\frac{2\pi z}{\Lambda}\right) \begin{cases} \frac{J_1(\lambda_1^+ r)}{J_1(\lambda_1^+ R_0)}, & r < R_0 \\ \frac{H_1^{(1)}(\alpha_1 r)}{H_1^{(1)}(\alpha_1 R_0)}, & r > R_0 \end{cases} \tag{25}$$

with $\lambda_1^+ = 0.0918145(2\pi/\Lambda)$, and

$$\begin{aligned} H_z(r < R_0) = &-\frac{i}{2\tilde{\omega}_0^2}\left[\frac{g_2^- J_1(\lambda_2^- r)}{J_1(\lambda_2^- R_0)} - \frac{g_3^- J_1(\lambda_3^- r)}{J_1(\lambda_3^- R_0)}\right] \\ &+\frac{i\sqrt{1+8\tilde{\omega}_0^4}}{2\tilde{\omega}_0^2}\left[\frac{g_2^- J_1(\lambda_2^- r)}{J_1(\lambda_2^- R_0)} + \frac{g_3^- J_1(\lambda_3^- r)}{J_1(\lambda_3^- R_0)}\right] \\ &-2i\sin\left(\frac{2\pi z}{\Lambda}\right)\left[\frac{g_2^- J_1(\lambda_2^- r)}{J_1(\lambda_2^- R_0)} + \frac{g_3^- J_1(\lambda_3^- r)}{J_1(\lambda_3^- R_0)}\right], \end{aligned} \tag{26}$$

$$H_z(r > R_0) = -2i\sin\left(\frac{2\pi z}{\Lambda}\right)\frac{(g_2^- + g_3^-)H_1^{(1)}(\alpha_1 r)}{H_1^{(1)}(\alpha_1 R_0)} \tag{27}$$

with $\lambda_2^- = i0.11834(2\pi/\Lambda), \lambda_3^- = 1.24157(2\pi/\Lambda), g_2^- = 0.592891, g_3^- = 0.128881$. Note that an accidental cancellation happens for the TE polarization such that $H_1^{(1)}(\alpha_0 r)$ vanishes. Using Eq. (21), this solution gives an overlap factor of $|\eta_u| \approx 0.1$.

B. 2D-Periodic Resonators

Dielectric ring resonators suffer from "inevitable" losses of photons due to their curvature and due to the sharp interfaces between domains of different indices of refraction. Both effects limit the maximum quality factor that can be attained in practice. Despite this, current state-of-the art resonators reach $Q \sim 10^6$ in periodically-poled (see Table 2 in Ref. [44]) and $\sim 10^4$ (see, e.g., Refs. [45, 46]) in periodically-grooved resonators *for circularly propagating modes*. As shown above, DM couples to standing wave-like modes with $\boldsymbol{K} \approx 0$, for which Q values are likely lower since they lie above the light-line $\omega = |\boldsymbol{K}|/n_{air}$ (i.e., these states can couple to continuum radiation). Photonic structures that are periodic in 2D, however, are known to support Bound States in Continuum (BIC) which are extremely long-lived modes with $|\boldsymbol{K}| \ll \omega$ [47]. We expect DM to couple most strongly to these $\boldsymbol{K} \approx 0$ modes.

The large Q values possible in BICs arise due to accidental cancellations between different radiation modes, or, due to a high degree of symmetry in the dielectric arrangement. In this section we explore the latter possibility by considering a dielectric slab with a square lattice of holes – see Fig. 3. The discrete rotational symmetry of the slab enables a categorization of all modes in terms of its irreducible representations (irreps) of the symmetry group; BICs and radiation modes fall into different irreps of the group, such that they formally have 0 overlap leading to a (formally) infinite quality factor [48]. In practice, the quality factor is controlled by the finite size of the slab, and manufacturing imperfections (e.g., variations in the size and positions of the holes), leading to realistic quality factors of 10^4 [37]. Even higher quality factors $\sim 5 \times 10^5$ have been engineered by tuning slab geometry to combine multiple BICs [49].

The device sketched in Fig. 3 consists of a square lattice of holes in the center serving as the resonator. The gaps ("line defects") surrounding the finite lattice act as highly effective (low loss) waveguides [50]. DM excites a standing wave mode in the resonator which leaks out into the gaps which guide the signal photons onto a detector.

The formalism described in Sec. II and the beginning of Sec. III applies to 2D-periodic structures. In fact, we can now slightly extend the previous discussion and allow for the resonator to be larger than a DM coherence length. This means that while individual unit cells still have a size much smaller than $\lambda_{\rm dB}$, their spatial separation can be much larger than $\lambda_{\rm dB}$. In this situation the overlap

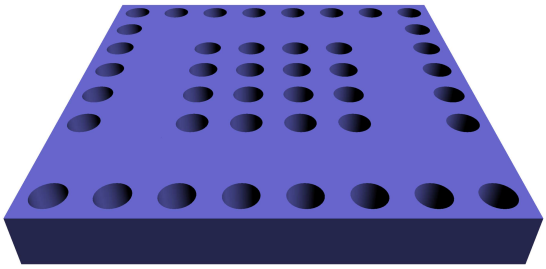

FIG. 3: A sketch of a photonic slab resonator (the periodic hole pattern in the middle) and the surrounding waveguides (gaps in the periodic hole pattern). For ease of illustration the resonator is drawn with only 16 unit cells. Wave-like DM can excite a mode in the resonator which sources fields in the waveguides.

factor can be written as

$$|\eta|^2 = |\eta_u|^2 \frac{1}{N_u^2} \sum_{i,j} e^{-i\boldsymbol{K}\cdot(\boldsymbol{R}_i - \boldsymbol{R}_j)} e^{-(\boldsymbol{R}_i - \boldsymbol{R}_j)^2/\lambda_{\rm dB}^2} \ , \quad (28)$$

which generalizes Eq. (12). This modification means that at a fixed $\boldsymbol{K}$ (correspondingly fixed ω), only those unit cells with $|\boldsymbol{R}_i - \boldsymbol{R}_j|/\lambda_{\rm dB} < 1$ contribute significantly to the overlap. By approximating the double sum in Eq. 28 by a double (two-dimensional) integral, it is straightforward to show that the result scales as $\lambda_{\rm dB}^2/(N_u A_u)$, such that the full signal power loses total volume scaling. Instead, for a fixed signal mode with Bloch momentum $\boldsymbol{K}$, the volume factor $V = N_u A_u h$ in Eq. 5 is effectively replaced by $\lambda_{\rm dB}^2 h$, i.e. the signal power appears to come from a single "coherence volume" of the detector. Extensive scaling of the signal power is restored if the detector is sensitive to a range of $|\boldsymbol{K}| \sim 1/\lambda_{\rm dB}$ values that the DM couples to. The result is that the signal power scales with total detector volume and Eq. 5 holds after summing over $\boldsymbol{K}$.[6]

Patterned slabs appear to have several useful features for DM detection. First, the effective index contrast between different regions within a unit cell is large, allowing us to maximize the overlap factor. Second, slabs feature a larger space-filling fraction on a substrate wafer, leading to a larger instrumented volume compared to, e.g., ring resonators on a same-sized wafer. Finally, the patterned slabs can have large areas $\sim$ cm^2 [37] at a single lattice spacing; alternatively, multiple slabs with different lattice spacings can be placed on a single line-defect

[6] This situation is completely analogous to the dielectric stack which has a much larger area than $\lambda_{\rm dB}^2$ [26]. As a result, the stack emits photons with a range of transverse momenta $\boldsymbol{k}_\perp$ as dictated the DM velocity distribution. The summation over these different modes is accomplished by the lens which redirects these photons onto a single detector. Only after this step the signal power proportional to the total area of the stack.

waveguide. The latter set-up is analogous to placing multiple ring resonators on a single bus. It would be interesting to study whether 3D-periodic structures have further advantages. We leave the exploration of DM signals in these systems to future work.

2D Example: Square Lattice of Holes

In this section we discuss some details of the square lattice photonic slab as a DM detector. Our primary aim is to show that this structure supports low-loss modes that couple to DM. The low loss condition implies that the signal mode does not couple to radiation modes, while a non-zero coupling to DM requires a non-zero overlap integral. We can gain insight into both requirements by considering symmetries of the slab.

The square lattice is symmetric under reflections about z plane and the point group C_{4v} [51], which consists of $\pi/2$ rotations, reflections through the xz, yz planes and through two other diagonal planes. In the idealized case of an infinite slab with perfect holes, the only losses are due to radiation above or below the slab, where the modes must reduce to plane waves propagating in $\pm z$. Since there are two polarizations, these radiation modes must correspond to two-dimensional irreps of C_{4v}. Therefore modes falling into one-dimensional (singlet) irreps (called A_1 and B_1) of C_{4v} cannot radiate to infinity. These are the low-loss modes we are after.

Now we can apply the condition of a non-zero overlap. This eliminates modes which are not symmetric under all reflections, leaving only A_1 irreps. Typically the mode with the largest overlap will have the fewest possible nodes, so we conclude that the lowest-energy A_1 will have the largest overlap factor. Such a mode is shown in Fig. 4 for slab height $0.5a$, hole radius $0.2a$ and slab dielectric constant $\varepsilon = 12$ where a is the length of the unit cell. This mode was found using `MPB` [52].[7] Numerically we find $\eta_u \approx 10^{-2}$. We leave the optimization of the overlap factor through variations in geometry to future work. It will also be interesting to explore other lattices.

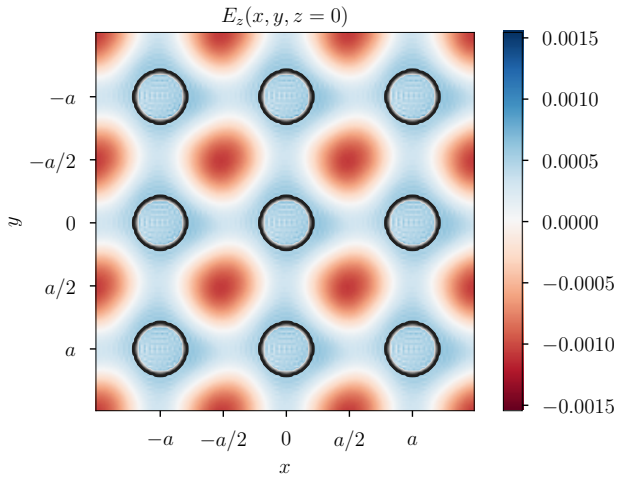

FIG. 4: Example electric field mode (in the $z = 0$ plane) of the square lattice of air holes that is both long-lived (symmetry-protected from coupling to radiation modes) and has a non-vanishing overlap with DM. The axes are given in units of the lattice constant a. The fields were found using `MPB` for slab height $0.5a$, hole radius $0.2a$ and slab dielectric constant $\varepsilon = 12$. The electric field amplitude is normalized to such that $\int d^3r\varepsilon|\boldsymbol{E}|^2 = 1$ over one unit cell. The black circles are the air holes in the dielectric slab. Only three periods of the photonic structure are shown in each direction.

IV. COMBINING SIGNALS

The optimal DM signal power that can be drawn from a signal resonator is proportional to the resonator volume. This volume is generically small for resonant frequencies $\omega \sim$ eV, required to search for DM with mass $m_{\rm DM} \sim$ eV. A large number of resonators is therefore needed to probe weakly-coupled DM at this mass. Fortunately, in photonic systems this is easily achieved with modern fabrication methods. However, care must be taken in the design to achieve the optimal combined signal. In this section we describe the basic criteria needed to do this, and identify several practical strategies. For a related discussion see Ref. [53].

The optimal signal power from N resonators is proportional to the total volume, since the collective system of N resonators may be equivalently considered to be a single resonator with N distinct cells. Thus N identical resonators have collectively an optimal power of NP_0, where P_0 is the optimal power of a single resonator. One might have thought that by combining signals in-phase an optimal power $\propto N^2$ could be achieved, but this is incorrect and it ignores the backreaction inherent in coupling power from a resonator with finite loss. Conservation of energy implies that the power input to the resonator by the DM source, the power lost to dissipation, and the signal power drawn from the resonator obey

$$P_{\rm source} = P_{\rm sig} + P_{\rm loss}. \tag{29}$$

For a resonator of quality Q driven by a fixed source current $\boldsymbol{J}_{\rm DM}$, on resonance we have that the source and loss power are determined by the resonator mode $\boldsymbol{E}_p$ and mode amplitude e_p as

$$P_{\rm source} = \frac{1}{2}\,{\rm Re}\left[e_p^* \int d^3x\; \boldsymbol{E}_p^* \cdot \boldsymbol{J}_{\rm DM}\right] \tag{30}$$

$$P_{\rm loss} = \frac{\omega|e_p|^2}{2Q} \int d^3x\; |\boldsymbol{E}_p|^2. \tag{31}$$

[7] https://github.com/NanoComp/mpb

Since these two quantities scale with different powers of e_p it follows that the signal power is bounded from above,

$$P_{\rm sig} \leq \frac{Q}{8\omega}\left(\frac{|\int d^3x\, \boldsymbol{E}_p^* \cdot \boldsymbol{J}_{\rm DM}|^2}{\int d^3x\, |\boldsymbol{E}_p|^2}\right) \equiv P_c \qquad (32)$$

which is saturated at a particular, critical value of the mode excitation $e_{\rm crit}$. This is essentially the result in Eqs. (5) and (7), save that those expressions further consider the microphysics of $\boldsymbol{J}_{\rm DM}$ generated by a stochastic DM field. Simultaneously reading out additional resonators does nothing to alter this bound, so long as the resonators are sufficiently separated that their presence does not alter the form of $\boldsymbol{E}_p$. Thus a system of N identical resonators can produce a signal power of at most NP_c.

A. Collective Readout

We now examine the requirements on a readout scheme to achieve the limit NP_c. Consider N identical resonators with no mutual interactions and assume that the DM coherence length is larger than the resonator size, but not necessarily larger than the distance between resonators. Let each resonator have a non-degenerate mode $\boldsymbol{E}_p$ with frequency ω_p and assume these modes are disjoint in space. Maxwell's equation may then be considered resonator-by-resonator, and the excitation e_i of the $i^{\rm th}$ resonator obeys

$$\left(\partial_t^2 + \frac{\omega_p}{Q}\partial_t + \omega_p^2\right) e_i\, \boldsymbol{E}_p = -e^{i\alpha_i}\partial_t \boldsymbol{J}_{\rm DM} \qquad (33)$$

$$\Rightarrow \quad e_i = \frac{-i\omega\, e^{i\alpha_i}}{\omega_p^2 - \omega^2 + i\frac{\omega\omega_p}{Q}}\left(\frac{\int_{V_i} d^3x\, \boldsymbol{E}_p^* \cdot \boldsymbol{J}_{\rm DM}}{\int_{V_i} d^3x\, |\boldsymbol{E}_p|^2}\right). \qquad (34)$$

Here we have taken $\boldsymbol{J}_{\rm DM}$ to represent the magnitude of the oscillating harmonic DM source of frequency ω, which is the same at each resonator location, and α_i is its phase which may vary between resonators.

The action of DM on this system of N resonators is nicely characterized by thinking of the system collectively as one oscillator possessing N-cells and an N-fold degenerate subspace of normal modes with frequency ω_p. The modes are labeled by the relative amplitude and phase of the field in each cell. Which of these normal modes does DM excite? It is to this mode that the readout must couple to draw the full available power.

If the DM coherence length is larger than the collective system, then the source phases are all equal $\alpha_i = \alpha_0$ and DM excites the uniform "0-mode" in which all resonators are excited with equal amplitude and phase. In this case we ought to couple the readout to all resonators identically. However, now consider the opposite limit in which the DM coherence length is smaller than the smallest inter-resonator spacing. In this case DM still excites one particular normal mode, that of equal amplitudes but non-equal phases $\{e^{i\alpha_i}\}$. As the α_i are unknown, we do not a priori know to which mode we ought couple. Further, after a coherence time $1/(m_{\rm DM}v^2) \sim {\rm ns}\,({\rm eV}/m_{\rm DM})$ the relative phases α_i change by $\mathcal{O}(1)$. In this case, the DM-driven normal mode is a moving target. In order to extract all of the power, we must simultaneously readout a complete basis of N normal modes.[8] A set of such modes acts as a net, catching all of the available DM power.

B. Single-mode Readout

An array of resonators coupled to a single output mode can only achieve complete coupling in the case of that DM is coherent over the full system. An example of such a readout is given in Fig. 6, in which one waveguide is coupled to N identical resonators in series. In this case the bus couples to one normal mode of the N-cell system, that which has a relative phase between consecutive cells matching the optical length of waveguide between those cells. In a single-mode readout of N incoherent resonators, the expected power is in fact independent of N and is equal to the power delivered by a single resonator, as we show here.

Consider an arbitrary readout mode with electric field

$$b\,\boldsymbol{E}_b\,(\boldsymbol{r}) = b\sum_i b_i \boldsymbol{E}_{p,i}\,(\boldsymbol{r})\,, \qquad (35)$$

where $\boldsymbol{E}_{p,i}$ is the mode function localized to resonator i and b is the overall mode amplitude. This mode may be labeled by a complex N-tuple of the relative amplitudes, $|b\rangle = (b_1, b_2, \ldots, b_N)$. How much power does this mode draw from the DM source? It obeys

$$\left(\partial_t^2 + \frac{\omega_p}{Q}(1+\gamma)\partial_t + \omega_p^2\right) b\,\boldsymbol{E}_b = -e^{i\alpha(r)}\partial_t \boldsymbol{J}_{\rm DM}, \qquad (36)$$

where we understand $\boldsymbol{J}_{\rm DM}$ to be spatially uniform and $\alpha(r)$ is a spatially varying phase such that $\alpha(r) = \alpha_i$ is a constant inside the $i^{\rm th}$ resonator. Note that the quality factor of the collective system is equal to that of an individual resonator. The coupling of power out of this mode is parameterized by γ, which we define to be the ratio of signal power to dissipated power. Thus

$$P_{\rm sig} = \frac{\omega\gamma}{2Q}\int_{\rm N} d^3r\, |b\boldsymbol{E}_b|^2, \qquad (37)$$

[8] In principle this does not need to be simultaneous. One could scan modes serially to identify the excited one and re-scan every coherence time. Such techniques are used in telecommunications, but it is unlikely they would be of use in a DM search where the signal is expected to be so weak that SNR $\gtrsim 1$ is only achieved after integrating longer than the coherence time.

where the integral is over the volumes of all N resonators. Since the modes are spatially disjoint and of equal amplitude, this is

$$P_{\rm sig} = \frac{\omega\gamma}{2Q}\langle b|b\rangle\,|b|^2\int_1 d^3r\,|\boldsymbol{E}_p|^2 \tag{38}$$

and the integral is now only over the volume of one resonator. The amplitude b follows from Eq. (36). Specialising immediately to the on-resonance case we have

$$b = \left(\frac{-iQ}{\omega_p\,(1+\gamma)}\right)\frac{\int_N d^3r\;\boldsymbol{E}_b^*\cdot\boldsymbol{J}_{\rm DM}e^{i\alpha(r)}}{\int_{\rm N} d^3r\,|\boldsymbol{E}_b|^2} \tag{39}$$

$$= \left(\frac{-iQ}{\omega_p\,(1+\gamma)}\cdot\frac{\int_1 d^3r\;\boldsymbol{E}_p^*\cdot\boldsymbol{J}_{\rm DM}}{\int_1 d^3r\,|\boldsymbol{E}_p|^2}\right)\frac{\langle b|\alpha\rangle}{\langle b|b\rangle}. \tag{40}$$

Here we have associated the DM source with an N-tuple of phases, $|\alpha\rangle = \left(e^{i\alpha_1}, e^{i\alpha_2}, \ldots, e^{i\alpha_N}\right)$. Note that the factor in parenthesis in Eq. (40) is the amplitude we would have in the case of a single resonator. The final signal power may be written

$$P_{\rm sig} = NP_c\frac{4\gamma}{(1+\gamma)^2}|\chi|^2 \tag{41}$$

where P_c is the maximal power that can be drawn from a single resonator, given in Eq. (32) and $|\chi|^2$ is an overlap factor between the readout mode $|b\rangle$ and the DM source mode $|\alpha\rangle$,

$$|\chi|^2 = \frac{1}{N}\frac{|\langle b|\alpha\rangle|^2}{\langle b|b\rangle}. \tag{42}$$

The signal power is maximized for $\gamma = 1$. The overlap χ is proportional to the projection of the DM mode onto the readout mode, and as such its maximal value occurs when these vectors are parallel,

$$|\chi|^2 \le \frac{\langle\alpha|\alpha\rangle}{N} = 1 \tag{43}$$

where $\langle\alpha|\alpha\rangle = N$ since it is a tuple of phases.

In the case of coherent DM, all α_i are equal and we may choose a single readout mode in which all b_i are equal, for example by spacing the resonators at integer multiples of the wavelength along the bus. It follows then that $|\chi|^2 = 1$ and the output power is optimal, $P_{\rm sig} = NP_c$. However, in the fully incoherent case, for a single readout mode we ought to take the b_i fixed and average over the α_i, which yields a suppressed overlap,

$$\langle|\chi|^2\rangle_\alpha = \frac{1}{N} \tag{44}$$

and thus $P_{\rm sig} = P_c$ for any fixed readout mode $\{b_i\}$.

C. Multi-mode Readout

In the incoherent case, the full power is recovered by reading out a full basis of normal modes. For any possible DM excitation mode, its overlaps with this set of readout modes will be sufficient to extract all of the power. To demonstrate this, suppose that one reads out an orthogonal set of modes $|c\rangle$ labeled by $c = 0, 1, \ldots N-1$, and each of these is critically coupled ($\gamma = 1$) to the output. Then the total output power is given by the sum of overlap factors,

$$\sum_c P_{\rm sig} = NP_c\sum_c |\chi\,(c)\,|^2, \tag{45}$$

and the sum of overlaps is 1, since it is a sum of projections onto an orthogonal basis, i.e.,

$$\sum_c \frac{|c\rangle\langle c|}{\langle c|c\rangle} = 1 \tag{46}$$

and the sum of overlaps is

$$\sum_c |\chi|^2 = \frac{1}{N}\sum_c \frac{\langle\alpha|c\rangle\langle c|\alpha\rangle}{\langle c|c\rangle} = 1 \tag{47}$$

which follows since $\langle\alpha|\alpha\rangle = N$. Thus the summed power is optimal, $\sum_c P_{\rm sig} = NP_c$.

V. PRACTICAL READOUT TECHNIQUES

There are many practical strategies by which the readout criteria discussed in Sec. IV can be achieved. A detailed implementation is beyond the scope of this work, however we will outline several techniques here to demonstrate the feasibility of complete readout over both coherent and incoherent systems. We will focus on the specific example of optical resonators placed along an output bus, as depicted in Fig. 6, however the techniques presented here are applicable to any multiple resonator system.

A. Coherent Spacing

First, as long as the typical linear size of the resonators R is smaller than $\lambda_{\rm dB}$, and taking the minimum spacing to be $\mathcal{O}\,(R)$, then any 2D block containing $\mathcal{O}\left(\lambda_{\rm dB}^2/R^2\right)$ resonators is driven by a coherent DM field. We may route an output bus through this block with path length between any two adjacent resonators being an integer multiple of the wavelength. For microring resonators, we typically have $R/\lambda \sim 100$ and so $\lambda_{\rm dB}/R \sim 10$. Such blocks occupy roughly 10 μm $\times$ 10 μm on the chip.

Beyond $\lambda_{\rm dB} \sim 10$ μm we have incoherence in the DM source, and we must implement a multimode readout. To conceptualize this, we may coarse-grain over the resonators in one coherence block and treat them as a single resonator coupled to the bus. The collection of such coherence blocks on the chip is thus equivalent to a set of incoherently driven resonators as studied above. To readout this system of N coherence blocks requires that we employ N readout modes coupled to a basis of the normal modes of the coherent blocks.

B. Spatial Combining

A simple approach to combining incoherent resonators is to allocate one bus per resonator and direct each of these buses to a separate detector. This amounts to choosing a "position basis" of readout modes: $(1, 0, 0, \dots)$, $(0, 1, 0, \dots)$, etc. This has the downside, however, of also increasing the total detector dark count rate by a factor of N. It is preferable to use one detector. Note that the buses cannot simply be fused before reaching the detector, as doing so hard-codes a relative phase between the signals from each pair of resonators and thereby actually implements a single-mode readout.

Instead, we can terminate each bus in an open, radiating end at the edge of the chip, and then place a photon counter close enough to the collect the radiation from all such buses, as illustrated in Fig. 5. This technique is an established way to couple signals off a chip [54, 55] and when used in this manner to combine signals it is an example of spatial or free-space power combining [56]. This readout is inherently multimode. If the normal mode excited by DM changes, then the phase of each emitter end will change and thus the outgoing radiation pattern changes. If the bus ends are located sufficiently far apart, then the radiation pattern implements a complete set of readout modes as a function of outgoing direction. We might imagine the signal emerging as a searchlight which is steered about in a stochastic way every DM coherence time. To collect the full signal power we then require a detector covering a sufficient solid angle as to be always intercepting this beam.

Now in reality a directed, searchlight beam is produced only in response to particular type of DM phase pattern, and the typical emission is a superposition of searchlights, each with different time-varying intensities. To see this, suppose that each bus is an integer number of wavelengths long, so that the emitting ends radiate with the same phase as the field in their respective resonators. We can then consider a "Bloch basis" of normal modes, labeled by a phase shift δ such that

$$|\delta\rangle = \left(1, e^{i\delta}, e^{2i\delta}, \dots, e^{i(N-1)\delta}\right), \tag{48}$$

i.e., each successive resonator is read with a phase δ relative to the prior resonator. This is an orthogonal basis if we take $\delta_c = 2\pi c/N$ for $c = 0, 1, \dots, N-1$. Each mode $|\delta\rangle$ will drive the emitters with a successive phase step of δ between them. This is exactly the configuration of a phased array antenna which emits a directed searchlight beam [57], and thus different modes $|\delta\rangle$ radiate a beamed signal with direction set by δ. If the emitters are spaced by l in a 1D array, then $|\delta_c\rangle$ emits into a finite number of lobes at directions

$$\sin\theta = \frac{2\pi}{kl}\left(m + \frac{c}{N}\right) \tag{49}$$

where θ is the angle away from the transverse to the array, k is the wavenumber of the signal radiation and m is an integer labeling the lobes for a fixed c.

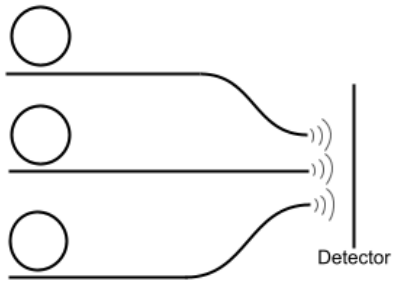

FIG. 5: Schematic depiction of spatial power combining of three identical resonators each coupled to their own output bus. The busses terminate with emitters and the resulting radiation is interfered in free space and collected on a nearby detector, resulting in complete multimode readout. For details see Sec. V B.

Consider the case of wide spacing $kl \gg 1$ and focus on the main lobes $m = 0$. Then $|\delta_c\rangle$ radiates into a direction

$$\theta_c \approx \frac{2\pi}{kl}\left(\frac{c}{N}\right). \tag{50}$$

The uniform mode $c = 0$ thus radiates forward and the other modes at slightly oblique angles $\mathcal{O}(1/kl)$. There is a series of such beams located farther off the forward direction, one for each m allowed by Eq. (50). Note the particular case of $kl = \pi$, for which there is exactly one lobe per mode c and these lobes together span $-\pi/2 < \theta < \pi/2$.

It follows that there are many specific arrangements of emitters that will yield an output power $\mathcal{O}(NP_c)$ for a detector covering an $\mathcal{O}(1)$ solid angle. The principle requirement is that by scanning θ we can correspondingly scan over all possible phase shifts between emitters, which is generically achieved so long as the emitters are spaced by roughly larger than one wavelength. Finally, note that sufficient detector coverage is possible even for small detector areas by simply placing the detector very near to the emitter ends. One might be concerned that the above discussion relied on far-field expressions like Eq. (50) while such a detector sits in the near-field region. However, in vacuum the total outward flux must be constant with distance, and so while the near-field radiation pattern may not exhibit the clear angular structure of Eq. (50) it is nonetheless the case that the power intercepted by the detector is $\mathcal{O}(NP_c)$.

C. Multiple Bus Modes

A different approach is to couple each normal mode $|c\rangle$ to radiation in the bus with a unique wavenumber $k(c)$. Scanning over wavenumber may then in principle scan over a basis of resonator modes and extract the full power. This has the advantage of allowing many identical

rings to share one bus and one detector, which increases the chip area available to resonators and minimizes the total dark count. There is one basic requirement to be met in this setup. If a full basis of normal modes couples to a set of bus modes spanning an interval of wavenumber Δk, then we must have that the frequencies of these bus modes span an interval less than the DM width $\Delta\omega/\omega \lesssim 10^{-6}$.

Consider an array of N identical resonators on a bus as in Fig. 6, with the resonators uniformly spaced by a distance d. Bus radiation of wavenumber k will couple to a "Bloch mode" $|\delta\rangle$ as in Eq. (48) with a phase step $\delta = kd$. In order to encompass a full basis $|c\rangle$ we take wavenumbers $k_c = 2\pi c/Nd$, i.e. $\Delta k \sim 2\pi/d$. We then require

$$\frac{\partial\omega}{\partial k}\left(\frac{2\pi}{d}\right) \lesssim \omega\, v^2. \tag{51}$$

For close-packed incoherent resonators $d > 1/mv$ and

$$\frac{\partial\omega}{\partial k} \lesssim v \sim 10^{-3}. \tag{52}$$

Thus the bus must support "slow light" modes, which precludes the use of an simple waveguide in which $\partial\omega/\partial k \sim 1$ [58]. The necessary dispersion may be engineered using periodic media or chains of coupled resonators [59].

For busses with relativistic dispersion $\partial\omega/\partial k \sim 1$ we might alternately engineer the phases of the bus-resonator couplings themselves to vary strongly with k, which allows a smaller range Δk to encompass a full basis. If we require $\Delta\omega \sim \Delta k \lesssim mv^2$, then we must have coupling phases ϕ which vary as

$$\frac{\partial\phi}{\partial k} \gtrsim \frac{2\pi}{mv^2}. \tag{53}$$

Additionally, we can consider techniques to increase the effective optical path length between the resonators, which also lowers the spread δk needed. One possibility is to couple the light into an intermediate, non-grooved microring where it would make many round trips before combining with the light from the subsequent rings. We leave a detailed study and optimization among these various techniques to future work.

VI. COUPLED MODE MODEL OF N RESONATORS IN SERIES

The most straightforward way to readout many resonators in a photonic system is to couple them in series along a single waveguide, as illustrated in Fig. 6. The outputs of these rings will interfere, and additionally the presence of the bus necessarily couples all rings together, violating one of the key assumptions of Sec. IV. The resulting response of the entire device to the DM source can be qualitatively different from that of non-interacting rings. In this section we derive the signal power from coupling N optical resonators "in series" following the coupled mode analysis of Ref. [60]. We will study the effects of resonator frequency and physical spacing, and their interplay with the coherence of the DM field. This verifies the ideas of Sec. IV in a more realistic setting, as well as accounts for the effects of mutual coupling.

We note that coupled arrays of optical resonators are well-studied in integrated photonics [61, 62]; in these applications the resonator array is usually excited from a single input port (one side of the bus) and the output is measured at the other end. For DM detection each ring acts as a possibly incoherent source of waves in the bus propagating in both directions, which requires a novel reformulation of the coupled mode theory [60].

Consider the setup as sketched in Figure 6 with N resonators of (potentially) different resonant frequencies ω_{R_l} coupled to a single bus. Since DM sources a standing wave in resonators with ω_{R_l} close to the DM mass, the signal photon can travel in either direction when it leaks to the receiver bus, and it can potentially excite neighbouring resonators. The field amplitudes a_l in this coupled system can be described by Coupled Mode Equations, which in frequency space read (following the notation of Ref. [60])

$$\left[i(\omega_{R_l} - \omega) - \tau_l^{-1}\right] a_l + \kappa_{1,l} s_{+1,l} + \kappa_{2,l} s_{+2,l} = s_{\mathrm{DM},l}, \tag{54}$$

where $s_{+1,l}$ ($s_{+2,l}$) are power amplitudes in the bus arriving from the left (right) at the lth resonator, $\kappa_{i,l}$ are the corresponding bus-resonator couplings, τ_l^{-1} is the resonator decay rate; $s_{\mathrm{DM},l} = s_{\mathrm{DM}}(\omega, \boldsymbol{x}_l)$ is the DM source at the position of each resonator which follows from Eq. 1:

$$s_{\mathrm{DM},l} = -\frac{\omega}{2\omega_{R_l}} \frac{\int d^3r \boldsymbol{E}_l \cdot \boldsymbol{J}^+_{\mathrm{DM}}(\omega, \boldsymbol{x}_l)}{\sqrt{\int d^3r \varepsilon \boldsymbol{E}_l^2}} \tag{55}$$

where $\boldsymbol{E}_l$ is the spatial profile of the ω_{R_l} mode in the lth resonator. The above system of equations, including the source term, follow from Maxwell's equations, Eq. (1), by taking the Fourier components of (real) EM fields near $\omega \approx \omega_{R_l} > 0$; $\boldsymbol{J}^+_{\mathrm{DM}}$ is the positive frequency part of the DM source, Eq. (68). We have assumed that the DM field is spatially-coherent over a single resonator, while allowing for different phases at different resonators; as a result $\boldsymbol{J}^+_{\mathrm{DM}}$ only depends on the position of the resonator, $\boldsymbol{x}_l$, but not on the integration over the resonator volume. The amplitudes a_l ($s_{+i,l}$) are normalized such that their time averages $\langle a_l(t)^2\rangle$ ($\langle s_{+i,l}(t)^2\rangle$) give the energy stored in the l'th resonator (power flowing through the bus at the l'th resonator).

The bus power amplitudes $s_{+i,l}$ couple all of the resonators together; in the weak coupling limit energy conservation allows us to express these quantities in terms of the mode amplitudes of other resonators on the bus:

$$s_{+1,l} = e^{-i\omega n_r d} \begin{cases} s_{+1,l-1} - \kappa^*_{2,l-1} a_{l-1} & l > 1 \\ 0 & \text{otherwise} \end{cases} \tag{56}$$

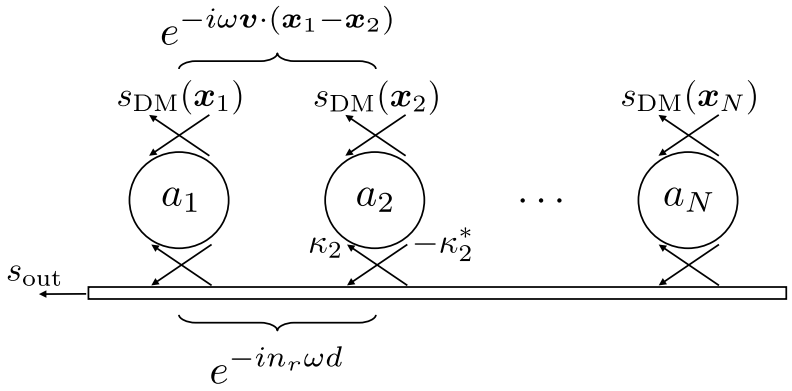

FIG. 6: N Resonators coupled to a single receiver bus with coupling κ_l, where the signal power amplitude $s_{\rm out}$ is read out at the end of the bus. The interaction between the dark matter and the resonators can be modelled as having N dark matter sources $s_{\rm DM}(\mathbf{x}_l)$ at each resonator, where $\mathbf{x}_l$ corresponds to the lth resonator's location. The separation between the resonators is d and the refractive index of the bus is n_r, which fix the relative phases between the DM sources, and the contributions of the different resonators to the power amplitude.

and

$$s_{+2,l} = e^{+i\omega n_r d}\begin{cases} s_{+2,l+1} - \kappa^*_{1,l+1}a_{l+1} & N > l \geq 0 \\ 0 & \text{otherwise} \end{cases} \tag{57}$$

where n_r is the effective refractive index of the receiver bus, d is the spacial separation between the neighboring resonators.

The symmetry of this configuration implies that the forward and backward bus-resonator couplings are equal

$$\kappa_l \equiv \kappa_{1,l} = \kappa_{2,l}. \tag{58}$$

They can be expressed in terms of an external quality factor $Q_{\rm e}$ as

$$|\kappa_l|^2 \equiv \frac{\omega_{R_l}}{2Q_{\rm e}}. \tag{59}$$

The total field amplitude decay rate τ_l^{-1} depends on these couplings and on the intrinsic resonator quality:

$$\tau_l^{-1} = \tau_{{\rm i},l}^{-1} + \tau_{{\rm e},l}^{-1} \tag{60}$$

where $\tau_{{\rm e},l}^{-1} = |\kappa_l|^2$ is the total partial width into bus modes propagating in either direction and

$$\tau_{{\rm i},l}^{-1} = \frac{\omega_{R_l}}{2Q_{\rm i}} \tag{61}$$

is the intrinsic loss rate. Note that decay rate of the mode energy $a_l(t)^2$ is $2\tau_l^{-1}$. The total or loaded quality factor includes both intrinsic and extrinsic losses

$$Q^{-1} \equiv Q_{\rm i}^{-1} + Q_{\rm e}^{-1} \tag{62}$$

and determines the physical width of the bus-coupled resonators.

We want to know the steady-state power that this system emits through the bus to the left or the right of all of the resonators; iterating Eq. 56 and Eq. 57 this output power amplitude is given by

$$s_{\rm out}(\omega) = \sum_{l=1}^{N} -\kappa_l^* a_l e^{-i\omega n_r d(l-1)} \equiv -\boldsymbol{t}\cdot\boldsymbol{a} \tag{63}$$

where

$$\boldsymbol{a} = (a_1, a_2, \cdots, a_N) \tag{64}$$

$$\boldsymbol{t} = \left(\kappa_1^*, \kappa_2^* e^{-i\omega n_r d}, \cdots, \kappa_N^* e^{-i(N-1)\omega n_r d}\right). \tag{65}$$

We can solve for $\boldsymbol{a}$ by inverting the linear system in Eq. 54:

$$\boldsymbol{a} = M^{-1}\boldsymbol{s}_{\rm DM} \tag{66}$$

where $\boldsymbol{s}_{\rm DM} = (s_{{\rm DM},1}, \ldots, s_{{\rm DM},N})$ and M is a symmetric matrix that captures the interactions among the resonators:

$$M = \begin{bmatrix} i(\omega-\omega_{R_1}) + \tau_1^{-1} & \kappa_1\kappa_2^* e^{-i\omega n_r d} & \cdots & \kappa_1\kappa_N^* e^{-i(N-1)\omega n_r d} \\ \kappa_1\kappa_2^* e^{-i\omega n_r d} & i(\omega-\omega_{R_2}) + \tau_2^{-1} & \cdots & \kappa_2\kappa_N^* e^{-i(N-2)\omega n_r d} \\ \vdots & \vdots & \ddots & \vdots \\ \kappa_1\kappa_N^* e^{-i(N-1)\omega n_r d} & \kappa_2\kappa_N^* e^{-i(N-2)\omega n_r d} & \cdots & i(\omega-\omega_{R_N}) + \tau_N^{-1} \end{bmatrix} \tag{67}$$

The time-averaged power emitted at the end of the bus is therefore

$$P_{\rm sig} = \frac{2}{T}\int_0^\infty \frac{d\omega}{2\pi}|s_{\rm out}(\omega)|^2, \tag{68}$$

where

$$|s_{\rm out}(\omega)|^2 = \sum_{ijkl} t_i M^{-1}_{ij} s_{{\rm DM},j} s^*_{{\rm DM},k} {M^{-1}}^\dagger_{kl} t^*_l \ . \tag{69}$$

Note that this spectral distribution is for signal radiated into one direction of the bus. If both ends of the waveguide are read out, then the total signal power is doubled.

As in the case of N non-interacting resonators, solved in Eq. (41), we have that the output power is given by the magnitude-squared of an overlap between a readout mode $\boldsymbol{t}$ and a DM source vector $\boldsymbol{s}_{\rm DM}$. However, Eq. (69) now includes the effects of interactions via M, and further it is expressed in terms of the amplitude-level couplings κ_l instead of the power ratios γ. The κ_l are more fundamental and depend only on the geometry, material properties and mode profiles of the resonator and bus, whereas the power drawn in a given setup will depend also on the amount of flux in the bus preceding the resonator.

Since the resonator spacing can be larger than the DM coherence length, the DM velocity dispersion is no longer negligible and $|s_{\rm out}(\omega)|^2$ will depend on the relative phases of the DM field at the different resonators. To obtain the expected steady-state output power we can average $|s_{\rm out}(\omega)|^2$ over possible DM field realizations for a given DM velocity distribution $f(\boldsymbol{v})$. Treating DM as a classical random Gaussian field, we find from Eqs. 55 and 2

$$\begin{aligned}\langle s_{{\rm DM},j} s^*_{{\rm DM},k}\rangle = &\frac{\omega^2}{4\omega_{R_j}\omega_{R_k}}\sqrt{V_j}\eta_{1,j}\sqrt{V_i}\eta^*_{1,k}\bar{J}^2_{\rm DM} \\ &\times \int d^3v f(\boldsymbol{v}) \exp i\left[m\boldsymbol{v}\cdot(\boldsymbol{x}_j - \boldsymbol{y}_k)\right] \\ &\times 2\pi T\delta(\omega - m)\end{aligned} \tag{70}$$

where η_j are the single resonator overlap factors

$$\eta_j = \frac{V_j^{-1}\int d^3r \boldsymbol{E}_j\cdot\hat{\boldsymbol{n}}}{\sqrt{V_j^{-1}\int d^3r \varepsilon \boldsymbol{E}_j^2}} \tag{71}$$

and $\bar{J}^2_{\rm DM}$ is given in Eq. (6). Note again that the DM field spatial dependence is taken outside of the single resonator overlap integral, Eq. (71), because we assume that DM is coherent over the resonator. The velocity distribution above is normalized such that $\int d^3v f(\boldsymbol{v}) = 1$; as in Section II we will take a Gaussian $f(\boldsymbol{v})$ for simplicity:

$$f(\boldsymbol{v}) = \frac{1}{\pi^{3/2}v_0^3} e^{-(\boldsymbol{v}+\boldsymbol{v}_\odot)^2/v_0^2}, \tag{72}$$

which allows to us to evaluate the velocity integral in Eq. 70 explicitly:

$$\begin{aligned}&\int d^3v f(\boldsymbol{v}) \exp i\left[m\boldsymbol{v}\cdot(\boldsymbol{x}_j - \boldsymbol{y}_k)\right] = \\ &\exp\left(-\frac{1}{4}m^2v_0^2(\boldsymbol{x}_j - \boldsymbol{y}_k)^2 - i\left[m\boldsymbol{v}_\odot\cdot(\boldsymbol{x}_j - \boldsymbol{y}_k)\right]\right)\end{aligned} \tag{73}$$

For the linear arrangement of resonators depicted in Fig. 6, $(\boldsymbol{x}_j - \boldsymbol{y}_k)^2 = (d|j-k|)^2$. Since $v_0 \sim |\mathbf{v}_\odot| \sim 10^{-3}c$, $\langle s_{{\rm DM},j} s^*_{{\rm DM},k}\rangle$ becomes exponentially suppressed when $\omega d|j-k| \gg 10^3$. In this limit, the DM source correlation matrix, Eq. (70), is proportional to the identity, corresponding to each resonator being incoherent with respect to its neighbours. However, as we will see in Section VII, we will need to maximize the number of resonators on a single bus while demanding that each resonator is of order the coherence length of DM (to maximize its volume). Thus we will be concerned with $d \sim 1/(mv_0)$ and some level of source correlation is inevitable between neighbouring resonators.

In order to develop intuition for the output power in Eqs. (69) and (70) we will apply them to $N = 1$ before presenting numerical results for large N.

A. One Resonator

Evaluating Eqs. (68) to (70) for $N = 1$ gives the total output power of a single resonator

$$P_1(m) = \frac{\tau_{\rm e}^{-1}\bar{J}^2_{\rm DM}|\eta|^2 V}{\omega_R^2}\frac{m^2}{(m-\omega_R)^2 + \tau^{-2}} \tag{74}$$

where we used $\tau_{\rm e}^{-1} = |\kappa|^2$ and added power radiated into both directions in the bus. On resonance, $m \approx \omega_R$, this becomes

$$P_{1,{\rm res}}(m) = \frac{2Q}{m}\left(\frac{\tau_{\rm e}^{-1}}{\tau^{-1}}\right)\bar{J}^2_{\rm DM} V|\eta|^2, \tag{75}$$

where Q is the loaded quality factor and $\tau_{\rm e}^{-1}/\tau^{-1}$ encodes the "branching fraction" of the resonator to decay into the bus. We define the ratio $\beta = \tau_{\rm e}^{-1}/\tau_{\rm i}^{-1}$ so that

$$\frac{\tau_{\rm e}^{-1}}{\tau^{-1}} = \frac{Q}{Q_{\rm e}} = \frac{\beta}{1+\beta} \tag{76}$$

Because $\tau^{-1} = \tau_{\rm i}^{-1} + \tau_{\rm e}^{-1}$, the signal power is maximized when $\tau_{\rm i}^{-1} = \tau_{\rm e}^{-1}$, i.e. $\beta = 1$. For this choice, Eq. (75) agrees with Eq. 5.

We will refer to *critical coupling* as any choice of κ_l that maximizes the power output of a given system. In general, the critical coupling depends on the number of resonator on the bus and their frequencies; moreover each resonator can have a different coupling, leading to a high-dimensional optimization problem for κ_l (see Appendices B and C). For simplicity we will focus on the case where all of these couplings are the same. Note that in general the ratio β, which is defined in terms of the amplitude-level couplings κ_l, is not the same quantity as the total power ratio γ used in Eq. (36). They coincide in the case of a single resonator, however for $N > 1$ they do not (see Appendix B).

B. N Resonators

While the system in Eq. (54) can be solved analytically for a few resonators, the general formulas are not enlightening, even for $N = 2$. Instead we study the solutions numerically and discuss special limiting cases. Our first goal is to investigate the N scaling of the signal power. As we will see it crucially depends on whether the resonators have equal resonant frequencies or not.

First, let us suppose that the $\omega_{R_l} = \omega_R$ for all l. In Fig. 7 we show the signal power as a function of relative detuning $(\omega_R - m)/\omega_R$ for different choices of N. The main conclusion that we draw from this figure is that peak power does not scale with N for generic choices of the resonator-bus couplings. The physical reason for this is that a signal photon produced by one resonator travelling down the bus can resonantly excite any of the other resonators and provides more opportunity for the photon to be lost. Specifically, the probability of a bus photon to resonantly excite a resonator and then to be lost due to internal losses is $\sim N\tau^2/(\tau_{\rm i}\tau_{\rm e})$ (unless it originates close to the end of the array, in which case, the N enhancement is absent). If $\tau_{\rm i} \sim \tau_{\rm e}$ then in this resonant regime $N \sim 1$ already leads to an $\mathcal{O}(1)$ probability for losing the signal photon! Naively, there are two ways out of this predicament. For example, if $\tau_{\rm e} \gg \tau_{\rm i}$ (and so $\tau \approx \tau_{\rm i}$), the loss probability is $N\tau_{\rm i}/\tau_{\rm e}$; so by varying $\tau_{\rm e}$ via the bus resonator couplings one can try to keep this probability small as N becomes large. This has two challenges: first, each resonator coupling needs to be adjusted based on its position in the array, leading to a high-dimensional optimization problem; second, taking $\tau_{\rm i}/\tau_{\rm e}$ small also shrinks the output power of each resonator (c.f., Eq. (75)) as $1/N$, so the overall N scaling is still lost, as we see in the $(\omega_R - m)/\omega_R \to 0$ corner of Fig. 7.

Another attempt is to consider the limit where $\tau_{\rm i} \ll \tau_{\rm e}$, i.e., internal losses are unimportant. In this regime, one can show that the output power on resonance is *exactly* that of a single resonator, see Appendix B. This has a simple intuitive interpretation in the fact that signal photons are trapped in the "bulk" of the array by being repeatedly re-absorbed by the different resonators; as a result the only photons that are detected come from resonators on either end of the array.

Both arguments about the lack of N scaling assumed that $m = \omega_R$; away from this resonant regime, the output power *does* grow with N, but the Q enhancement is lost.[9] Thus there appears to be no advantage of having resonators of the same frequency coupled to a single bus with fixed phase, as in the model of Eqs. (54) and (63). In this setup only a single normal mode of the entire system is read out. As discussed in Sections IV and IV C a multimode read out can restore the extensive N scaling.

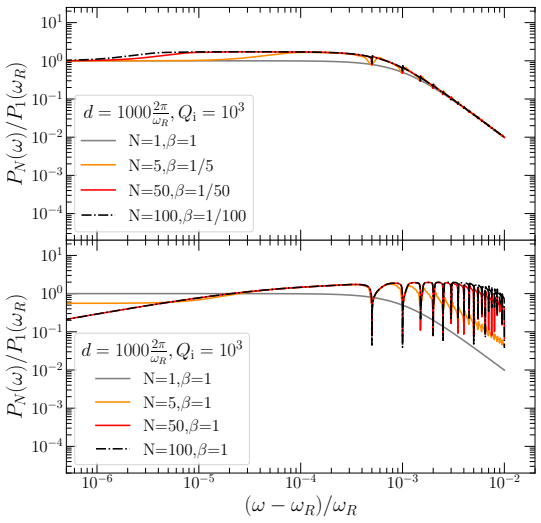

FIG. 7: The power drawn from N resonators with the *same frequency* on one bus (Eq. (68)), normalized by $P_{\rm res,1}$, the peak power from a single critically-coupled resonator (Eq. (75)). β is the coupling ratio defined in Eq. (76), taken to be 1 in the bottom panel, and critical for N coherently spaced resonators in the top panel, however these have spacing d which is beyond coherence.

We now consider the case where all the resonance frequencies are different, drawn from the set

$$\omega_{R_l} \in \{\omega_R(1+\delta)^{i-1} \;\mid\; i \in [1..N]\} \tag{77}$$

where ω_R is the lowest target frequency in the series and δ is a fractional frequency change between neighbouring frequencies (these frequency space neighbours do not need to be neighbours in position space). Since we are interested in covering a region of DM mass range without gaps, we will consider $\delta \sim$ few $\times\, Q^{-1}$. Because no two resonators have the same resonant frequency, the response of the coupled system is approximately the sum of responses of N uncoupled resonators. This can be easily seen from the structure of Eqs. (67) to (69): at a given driving frequency ω only one of the diagonal entries in Eq. (67) is large, so the output power approximately decomposes into a sum over different resonators. This decomposition is nearly exact when the resonators are spaced by more than a de Broglie wavelength; otherwise non-trivial source phase correlation can play a role in determining the precise response, especially if the neighbouring resonators in physical space also have similar frequencies, as illustrated in Fig. 8. It is clear that the signal bandwidth grows with N as $N\delta\omega_R$, enabling a broadband DM search in all three cases. The ordered arrangement corresponds to the resonators arranged sequentially according to frequency, i.e., $\omega_{R_l} = \omega_R(1+\delta)^{l-1}$. For the

[9] N scaling is also present if all N resonators are within a single DM coherence length (see Appendix B); this, however, means that each resonator has a volume that is a factor $\sim 1/N$ smaller than it could be.

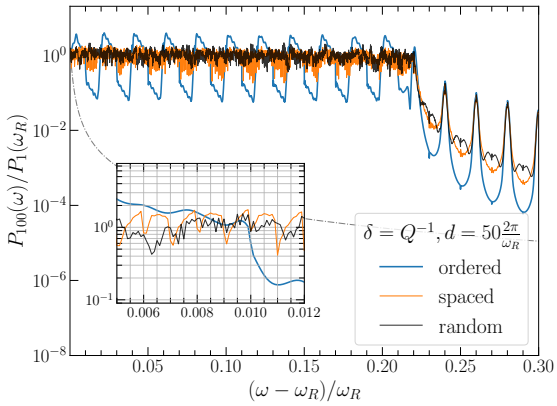

FIG. 8: Power output from $N = 100$ resonators in series with three different spacial arrangements of resonant frequencies from the set in Eq. (77). Each resonator has a quality factor of $Q = 500$. $P_1(\omega_R)$ is the peak power from a single resonator. The total signal bandwidth is given by $\sim N\omega_R/Q$. For comparison, $P_1(\omega)/P_1(\omega_R)$ is shown in a gray dashed line. The spacing between resonators is less than the coherence length, which gives rise to the clear structure in the ordered case. When the resonators are randomized or spaced according to Eq. (78) this structure disappears as all resonators with similar frequencies are then incoherent.

spaced arrangement neighbouring frequencies are separated in space by 10 positions; this is implemented by taking $\omega_{R_l} = \omega_R(1+\delta)^{g(l)-1}$, where

$$g(l) = \begin{cases} \lfloor \frac{l}{10} \rfloor + \frac{N}{10}((l \bmod 10) - 1) + 1 & l \bmod 10 \neq 0 \\ (l + 9N)/10 & l \bmod 10 = 0 \end{cases} \tag{78}$$

assuming N is a multiple of 10. For example, the first resonator has $\omega_{R_1} = \omega_R$, while the next frequency appears at $l = 11$, i.e., $\omega_{R_{11}} = \omega_R(1+\delta)$. Finally, the random arrangement allocates frequencies from (77) to the resonators randomly. It can be seen that the power becomes more evenly distributed among all frequencies within the bandwidth using a random or spaced arrangement compared to an ordered arrangement. This is because a small separation in frequencies between nearby resonators enables interference effects if they are within the DM coherence length. Therefore, the random or variations of the spaced arrangement of frequencies are preferred to ensure a "smooth" detector response.

For the randomly spaced array the peak power for a DM mass within the bandwidth of the resonator array is simply given by Eq. (75).

VII. PROJECTED SENSITIVITY

We now use the insights developed in the previous sections to project the sensitivity of realistic experimental setups to the axion-like particle and dark photon models. We will use the language of microring resonators, but our estimates are valid for any other resonator formfactor (e.g., slabs and other types of photonic crystal cavities) only with different numerical factors that encode their volumes, overlap factors, filling fractions, etc. Integrated high Q resonators have been demonstrated across various spectral regions including the visible [63], near-infrared [44], mid-infrared [64, 65], and long-wave infrared [66] domains, corresponding to photon wavelengths from 0.4 μm to 11 μm. Therefore, we estimate the sensitivity of photonic devices to DM with masses from 0.11 to 3 eV. Different resonator materials and photon detectors will be required to cover this mass range.

A. Signal Rate

First let us estimate the signal rate from a single microring resonator with the target frequency ω_R. The largest overlap factors are expected to arise from the EM modes with fewest nodes, which means that the length of a single unit cell is approximately $2\pi/\omega_R$, leading to a resonator circumference of $L = 2\pi/\omega_R \times N_u$ where N_u is the number of unit cells. The cross-sectional area of the resonator is $A = t_w \times 2\pi/\omega_R$, where t_w is the thickness of the waveguide. Using Eq. (75) with Eq. (6), the signal rate from one critically-coupled ($\tau_e^{-1} = \tau^{-1}/2$) resonator on resonance is

$$\Gamma_1(\omega_R) \sim \frac{10^{-11}}{\text{sec}} \times \begin{cases} 0.2\left(\frac{0.25\text{eV}}{\omega_R}\right)^4 \left(\frac{g_{a\gamma}\text{GeV}}{10^{-10}}\right)^2 \left(\frac{B}{9.4\text{T}}\right)^2 \\ 10^9 \left(\frac{0.25\text{eV}}{\omega_R}\right)^2 \left(\frac{\chi}{10^{-10}}\right)^2 \end{cases} \tag{79}$$

where $Q = 5000$, $|\eta_u|^2 \sim 0.1$, $N_u = 100$, $t_w = 10$ μm. Here the first (second) line corresponds to axion (dark photon) DM. For both models, the coupling ($g_{a\gamma}$ or χ) has been normalized to a value near the current experimental bounds [67, 68]. Note that the signal rate for dark photon DM is significantly higher than that of axion DM in this mass range, due to the relatively weaker solar constraints at these masses. Even over one year, the number of events in a single resonator from axion DM at currently allowed couplings is significantly less than 1. To increase this reach signals from a large number of resonators need to be combined.

At a single frequency, resonator power may be summed using the techniques discussed in Section V. For concreteness we consider here the use of spatial power combining, however the parametrics of the signal power depend only on the number of resonators and not the adding mechanism. Thus in practice other techniques may be used as well. In addition, to search a mass interval of fractional width larger than $1/Q$ it is necessary to employ

resonators of different frequencies, either by building different sets of wafers or by including multiple resonant frequencies within one wafer. Indeed we can vary the frequency along a single bus, as there are no strong destructive interference effects between signals of differing frequency. See Fig. 8 for a study of this arrangement. We do not optimize here the frequency coverage per wafer, as this ought to consider various factors beyond the scope of this work, such as the overhead of fabrication and install as well as the fact that using multiple frequencies alleviates some of the challenges of power combining as we have fewer common-frequency resonators to sum. We instead consider here a reasonable example setup, depicted in Fig. 1, where a number of coupled resonator series are laid out in parallel. In each series, a given resonant frequency appears only once, but the same resonant frequency appears many times over an entire wafer in different series. Each series is then combined with a spatial combiner.

We will now estimate the number of resonators that can be reasonably packed onto a single wafer and use that to evaluate the bandwidth and sensitivity of such a device. In a wafer of diameter D, the number of resonators that can be placed in a series is $N \sim D/d$, where d is the separation between the resonators. Parametrizing $d = l \times 2\pi/\omega_R$, the resonators do not overlap in space if $l > N_u/\pi$. The resonator targeting the lowest frequency ω_R in each series has the largest size, so it determines the number of series that can be placed in parallel on the wafer. For a microring, the width w of a single series is at least the sum of the width of the receiver bus and the diameter of the microring, i.e., $w \gtrsim (N_u/\pi + 1)\,(2\pi/\omega_R)$. Thus, approximately D/w series systems can be accommodated on a wafer; assuming the series are identical, D/w is also the number of resonators with any particular target frequency ω_{R_i}, N_ω. The (resonant) signal rate at each of these target frequencies is $N_\omega \Gamma_{\rm sig}(\omega_{R_i})$ where $\Gamma_{\rm sig}$ is given in Eq. (79). Moreover, since there are D/d different target frequencies the bandwidth of a single device is greatly enhanced. For example, a single 150 mm diameter wafer can accommodate $D/d \sim D/w \gtrsim 10^3$ series and resonators per series for $w \sim d \sim 100\ \mu$m.

Despite large single-wafer enhancement factors, experiments seeking discover DM beyond existing constraints must instrument larger volumes by combining multiple wafers. For axion DM searches a major limiting factor is the magnetic field volume. With this in mind, it is useful to compute the total interaction volume which will be constrained by magnet size or other practical considerations. Since the volume of a single ring is $LA \approx N_u \left(\frac{2\pi}{\omega_R}\right)^2 \times t_w$, the effective interaction volume for a single wafer targeting frequencies $[\omega_R, \omega_R(1+\delta)^{N-1}]$ is

$$V_{\rm int} \approx LA\frac{D^2}{dw} \lesssim \frac{D^2 t_w \pi}{(N_u/\pi + 1)} \sim \frac{D^2 t_w \pi^2}{N_u}, \tag{80}$$

which is *independent* of the base frequency ω_R. The integrated components form a thin layer on a wafer, so the "active" volume fraction is small:

$$\xi_{\rm act} \equiv \frac{V_{\rm int}}{\pi D^2 t_s/4} \sim 0.1\% \left(\frac{100}{N_u}\right)\left(\frac{t_w/t_s}{0.01}\right), \tag{81}$$

where t_s is the thickness of the wafer. Since $\xi_{\rm act}$ is independent of the wafer size and target frequency range, the total signal rate is enhanced by a factor corresponding to the total number of resonators per frequency,

$$\Gamma_{\rm sig} \approx 4 \cdot 10^7\, \Gamma_1 \left(\frac{100}{N}\right)\left(\frac{V_{\rm act}}{100\ {\rm cm}^3}\right) \times \\ \times \left(\frac{\omega_R}{0.25\ {\rm eV}}\right)^2 \left(\frac{100}{N_u}\right)\left(\frac{10\ \mu{\rm m}}{t_w}\right) \tag{82}$$

where Γ_1 is given in Eq. (79). The maximum possible active volume $V_{\rm act}$ in any axion search is controlled by $\xi_{\rm act}$ times the magnet bore volume. In Table I we list several strong, large-bore magnets that either exist or are being considered. It is clear that larger bore sizes generally yield a bigger $B^2 V_{\rm act}$. Given a fixed $B^2 V_{\rm act}$ that covers N axion frequencies, the axion DM signal rate becomes

$$\Gamma_{\rm sig}(\omega_R) \sim \frac{8\times 10^{-5}}{\rm sec}\left(\frac{Q}{5000}\right)\left(\frac{|\eta|^2}{0.1}\right)\left(\frac{0.25\ {\rm eV}}{\omega_R}\right)^2 \\ \left(\frac{g_{a\gamma}{\rm GeV}}{10^{-10}}\right)^2 \left(\frac{B^2 V_{\rm act}}{4.2\times 10^7\ {\rm PeV}}\right)\left(\frac{100}{N}\right). \tag{83}$$

B (T)	Bore (mm)	$V_{\rm act}$ (cm^3)	$B^2 V_{\rm act}$ (PeV)	References
40	34	9×10^{-3}	6.9×10^4	[69]
21	123	0.118	2.5×10^5	[70]
9.4	800	100	4.2×10^7	[71]
11.7	900	127	8.3×10^7	[72]
20[a]	680	72.6	1.38×10^8	[73]

[a] A future 20 Tesla MRI magnet

TABLE I: Realistic magnet parameters that can be employed in an axion search. All entries are MRI magnets except for the 40 Tesla magnet. $V_{\rm act}$ is the product of the physical volume of the bore and the active fraction $\xi_{\rm act} \sim 0.1\%$, defined in Section VII A.

B. Background

The coupling reach is enhanced if a larger active volume (i.e., larger $\xi_{\rm act}$) can be obtained. This can be achieved by decreasing the thickness of the wafer and increasing the thickness of the integrated structures. One concern in doing so is that this increases the number of readout buses and thus the number of detector elements needed for full spatial readout. In a given run, the de-

tector area needed is

$$A_{\rm d} \approx 40\ {\rm cm}^2 \left(\frac{V_{\rm act}}{100\ {\rm cm}^3}\right)\left(\frac{10\mu{\rm m}}{t_w}\right)\left(\frac{100}{N_c}\right)\left(\frac{100}{N_u}\right) \tag{84}$$

where N_c is the number of coherently-spaced resonators of the same frequency along each bus.

We consider two example detector systems, Skipper charge-coupled device (CCD) and superconducting nanowires (SNSPDs) [32]. The relevant properties are listed in Table II. Over our full detector area (84) we have a dark count timescale of

$$\left(\frac{V_{\rm act}}{100\ {\rm cm}^3}\right)\Gamma_{\rm bkg}^{-1} \approx \begin{cases} 40\,{\rm sec}, & \omega < 1.12{\rm eV\ (SNSPD)} \\ 60\,{\rm sec}, & \omega > 1.12{\rm eV\ (CCD)}. \end{cases} \tag{85}$$

C. Reach

The signal-to-noise ratio of a given run with integration time $t_{\rm int}$ is

$${\rm SNR} = \frac{\Gamma_{\rm sig} t_{\rm int}}{{\rm Max}\left[1, \Gamma_{\rm bkg} t_{\rm int}\right]^{1/2}} \tag{86}$$

where the 1 in the denominator corresponds to a background-free run.

We consider multiple runs, each of which use a unique set of resonators targeting a different frequency window $[\omega_R, \omega_R(1+\delta)^{N-1}]$ where $\delta = 1/Q = 2\cdot 10^{-3}$ and $N = 100$. Therefore, the relative bandwidth in each run is $\sim N\delta = 0.2$, which is significantly larger than that of the DM source bandwidth, enabling broadband detection (i.e., each run is sensitive to a wide range of DM masses). Note that for simplicity we assumed N is the same in each run; however, as the target frequency range varies, so does the physical size of the resonators and N can in principle be optimized to maximize the scan sensitivity in each frequency range. The number of runs needed to cover a frequency range (ω_1, ω_2) is

$$N_{\rm scans} \approx \frac{1}{N\delta}\log\left(\frac{\omega_1}{\omega_2}\right). \tag{87}$$

For example, as shown in Fig. 9, for $Q = 500$ and $N = 100$ and a total integration time per photodetector technology of one year, we cover the range between $0.1\ {\rm eV} < \omega < 1.12\ {\rm eV}$ using SNSPDs in 12 runs and between $1.12\ {\rm eV} < \omega < 2\ {\rm eV}$ using CCDs in 4 runs. We let each run to integrate for

$$t_{\rm int} \approx \begin{cases} 2.6\cdot 10^6\ {\rm sec}, & \omega < 1.12\ {\rm eV\ (SNSPD)} \\ 6.4\cdot 10^6\ {\rm sec}, & \omega > 1.12\ {\rm eV\ (CCD)}. \end{cases} \tag{88}$$

Assuming a given magnet bore can be completely instrumented with wafers populated by resonators as described above, these integration times yield an axion-photon coupling sensitivity of

$$\begin{aligned} g^*_{a\gamma} \approx& \frac{2\omega}{\sqrt{\rho_{\rm D}}}\sqrt{\frac{N}{B^2 V_{\rm act} Q|\eta_u|^2}}\left(\frac{1}{t_{\rm int}\Gamma^{-1}_{\rm bkg}}\right)^{1/4} \\ \approx& \frac{7\times 10^{-11}}{\rm GeV}\left(\frac{\omega}{0.25\ {\rm eV}}\right)\left(\frac{1\,{\rm month}}{t_{\rm int}}\right)^{1/4}\left(\frac{40\ {\rm sec}}{\Gamma^{-1}_{\rm bkg}}\right)^{1/4} \\ & \left(\frac{4.2\cdot 10^8\ {\rm PeV}}{B^2 V_{\rm act}}\right)^{1/2}\left(\frac{500}{Q}\right)^{1/2}\left(\frac{N}{100}\right)^{1/2}\left(\frac{0.1}{|\eta_u|^2}\right)^{1/2}. \end{aligned} \tag{89}$$

Note that while we expressed the reach in terms of the total active volume, the actual volume inside the magnet bore dedicated to a particular target frequency is $V_{\rm act}/N$ where N is the number of different target frequencies in every series. We assumed the 9.4 T magnet in Table I as an example, but other large bore MRI magnets all have similar $B^2 V_{\rm act}$ and would therefore result in comparable sensitivity.

We conclude this section by discussing the sensitivity of similar experiments to dark photon DM. Unlike searches for axion-like particles, dark photon experiments do not need a strong magnetic field. Therefore the key experimental parameter is simply the active volume of the detector. Note that this implies that the dark count is a function of active volume, too. Unlike the background-dominated regime in Eq. (89), dark photon dark matter search can be quite sensitive already in a background free regime, where the kinetic mixing sensitivity is approximately

$$\begin{aligned} \chi^* \approx& \sqrt{\frac{12N}{Q\rho_{\rm D} V_{\rm act} t_{\rm int}|\eta_u|^2}} \\ \approx& 10^{-13}\left(\frac{10^4\ {\rm sec}}{t_{\rm int}}\right)^{1/2}\left(\frac{0.1\ {\rm cm}^3}{V_{\rm act}}\right)^{1/2} \\ & \times\left(\frac{N}{100}\right)^{1/2}\left(\frac{500}{Q}\right)^{1/2}\left(\frac{0.1}{|\eta_u|^2}\right)^{1/2}. \end{aligned} \tag{90}$$

In Fig. 10 we project the experimental reach for different choices of $V_{\rm act}$ and $t_{\rm int}$.

VIII. CONCLUSION

The landscape of dark matter models is extremely broad, covering many orders of magnitude in mass range. As a result, discovering these different possibilities requires a varied set of experimental techniques. In this paper we have explored the interactions of DM with integrated photonic systems and showed that ambient DM with couplings to electromagnetism can resonantly excite photonic devices if they have periodic variations in their

Detector	Range (eV)	DC (sec^{-1})	Size (μm^2)	Refs.
SNSPD	$0.1 - 1.12$	$6 \cdot 10^{-6}$	400×400	[27, 74]
CCD	$1.12 - 3$	10^{-9}	15×15	[75]

TABLE II: Detector technologies considered here. Columns show the frequency range we study, dark count rate and physical collecting area per element, and relevant references. The threshold energy 1.12 eV is the bandgap of silicon. Signal photons below the bandgap must be detected with SNSPDs, while those above can be observed with skipper CCDs.

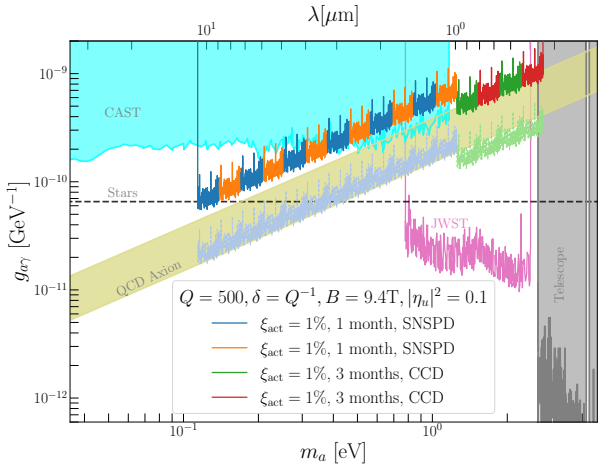

FIG. 9: Projected sensitivities to the axion-photon coupling $g_{a\gamma}$, assuming SNR=1 (86). Each scan is represented by one of the blue, orange, green and red lines, and requires filling the magnet bore with systems of $N = 100$ resonator series, with a bandwidth $\Delta_{\text{sig}}/\omega_R \sim \delta N$. The magnetic field B is provided by the 9.4 T magnet listed in Table I. ξ_{act} given by (81) indicates the percentage of the volume inside the magnet that contributes to the axion-photon interaction. A total of approximately 2 years is required to cover the mass range covered. The lighter dashed lines take $Q = 5000$ for each scan and thus would require 10 times more time to cover the same mass range. The QCD axion is indicated by the yellow band. Also shown are existing bounds from helioscope searches [76], stellar evolution [77, 78], and indirect detection [79–81].

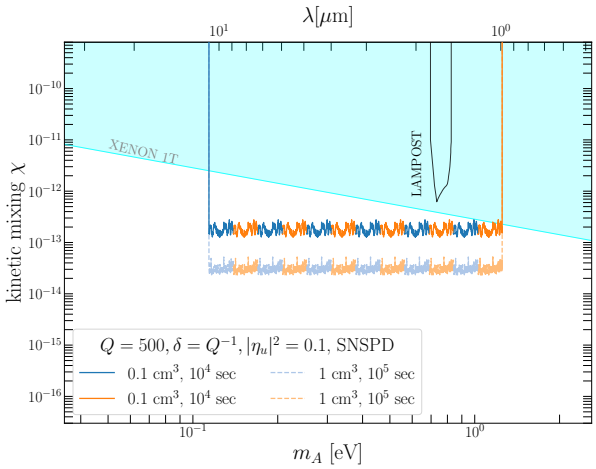

FIG. 10: Projected sensitivities to the photon-dark photon kinetic mixing χ assuming SNR=1 (86). Each solid (dashed) scan assumes an interaction volume of 0.1 cm^3 (1cm^3) and an integration time of 10^4 sec (10^5 sec). The entire volume is filled with systems of $N = 100$ resonator in series targeting different frequency ranges, each with bandwidth $\Delta_{\text{sig}}/\omega_R \sim \delta N$ with $\delta = 1/Q$. Also shown are existing limits from searches for solar-produced dark photons with Xenon1T [82] and the DM search LAMPOST [27].

structure. As a result, this technology can enable discovery of DM with masses near the electronvolt scale. This work is a major foray into the use of integrated photonics for fundamental physics, and represents a promising new avenue for DM searches.

We argued that attaining leading sensitivity to DM models in this mass window typically requires coupling a large number of resonators together, making integrated photonic circuits an ideal laboratory for such searches. These systems introduce unique challenges and opportunities for DM experiments. For example, by solving the coupled mode equations of the system we showed that its response to the DM source is qualitatively different than that of uncoupled resonators. This fact, combined with the novel sensitivity of these detectors to the phase of the DM field across the device suggest that the simplest searches involve multiple resonators at slightly different frequencies, leading to a broadband sensitivity to a range of DM masses at once. Moreover, because the signal photons are collected in wavelength-scale waveguides, they can be counted with small, extremely low dark-count photodetectors, like superconducting nanowires and Skipper charge-coupled devices. Our projections show that such a set-up can easily surpass existing limits on DM and test theoretically-interesting parameter space (e.g., the QCD axion mass-coupling relation). These results are summarized in Figs. 9 and 10.

While our forecasts drew on detailed results from coupled mode theory, we have not optimized many of the experimental specifics. For example, we have discussed only two possible implementations of photonic resonators as (one-dimensional) periodic microrings or (two-dimensional) photonic slabs. Moreover, we made simplifying assumptions about the coupling of each resonator to the read-out bus which plays a key role in determining the response of the entire system. For example, in the microring case, the geometry of the ring-bus coupling region can be chosen to maximize the proba-

bility of successfully collecting a signal photon. We also showed that the simplest implementation of the coupled resonators idea results in a read-out that is only sensitive to a single normal mode of the system. We can achieve near-extensive scaling of signal-to-noise with device count N using spatial read-out of all normal modes, however it may be possible to achieve a fully extensive scaling by coupling all such modes into a single read-out bus. Such a device can be used to study a narrow range of frequencies in the case of a signal from the broadband approach. We leave these exciting considerations to future work.

Integrated photonic devices also provide novel opportunities compared to other experiments. For example, their DM response can be experimentally characterized by exciting the DM-coupled modes with a transverse laser beam, which is difficult to do in other configurations such as the dielectric stack. In the event of a null result, this would enable a precise mapping of the constraints onto the DM parameter space. As mentioned above, different resonators in the system are probing different DM phases. It would be interesting to develop a phase-sensitive read-out scheme to extract information about the local DM velocity distribution in the event of a signal. Finally, the resonators can be constructed out of non-linear materials such as lithium niobate which can enable novel DM search channels using active/excited resonators, such as photon up- or down-scattering. Integrated photonics thus provides a very rich platform for ultralight DM searches.

ACKNOWLEDGMENTS

Acknowledgments. We thank Yoni Kahn, Alex Millar, Masha Baryakhtar, Junwu Huang, Daniel Egana-Ugrinovic, Asher Berlin, and Albert Stebbins for helpful discussions. This work is supported by the DOE QuantISED program through the theory consortium "Intersections of QIS and Theoretical Particle Physics" at Fermilab. Fermilab is operated by the Fermi Research Alliance, LLC under Contract DE-AC02-07CH11359 with the U.S. Department of Energy. RH and RJ are also supported by the U.S. Department of Energy, Office of Science, National Quantum Information Science Research Centers, Superconducting Quantum Materials and Systems Center (SQMS) under contract number DE-AC02-07CH11359. CG and RH also acknowledge the Aspen Center for Physics for its hospitality where part of this work is done, which is supported by National Science Foundation grant PHY-1607611.

Appendix A: Dark Matter Field and Signal Coherence

In this Appendix we relate the (known) DM velocity distribution to the statistical properties of the DM source that appears in Eq. (1). We use this to derive the generic expression for DM signal power including coherence effects that appears in Eqs. (5) and (7). Here we refer to the DM as axions, but completely analogous reasoning applies to dark photon DM.

1. DM as a Random Field

It is known in optics that the density operator

$$\hat{\rho} = \Pi_i \hat{\rho}_i = \Pi_i \sum_{n_i} \frac{\langle n_i \rangle^{n_i}}{(\langle n_i \rangle + 1)^{n_i+1}} |n_i\rangle\langle n_i| \tag{A1}$$

where the summation runs over all the modes, applies not only to the thermal photon distribution but also a wide range of excitations in which the statistical properties of the light are suitably random [83]. Since the axion dark matter is stochastic, (A1) could be a good description. Given an axion field operator

$$\hat{\phi}(\mathbf{x}, t) = \sum_{l=1}^{N} \frac{1}{\sqrt{2\omega_l V}} \left(\hat{a}_l e^{i\mathbf{x}\cdot\mathbf{k}_l - i\omega_l t} + h.c. \right) = \hat{\phi}^+ + \hat{\phi}^- \tag{A2}$$

where $\omega_l \simeq m + \frac{1}{2} m v_l^2$, we can compute observables using $\langle \mathcal{O}(\phi) \rangle = \mathrm{Tr}\left(\rho \hat{\mathcal{O}}(\phi)\right)$. If $n, \langle n \rangle \to \infty$, the probability $P(n)$ approximately takes the following form

$$P(n) = \frac{1}{\langle n \rangle + 1} \left(1 - \langle n \rangle^{-1}\right)^n \approx \frac{1}{\langle n \rangle} e^{-n/\langle n \rangle}. \tag{A3}$$

Let us compute $\langle \hat{\phi}(\mathbf{x}, t) \hat{\phi}(\mathbf{x}', t') \rangle$ in the large $n, \langle n \rangle$ limit, corresponding to the regime in which can think of ϕ as a classical field:

$$\begin{aligned} &\langle \hat{\phi}^-(\mathbf{x}, t) \hat{\phi}^+(\mathbf{x}', t') \rangle \\ &= \sum_l \frac{1}{2\omega_l V} \langle n_l \rangle e^{-i\mathbf{k}_l \cdot (\mathbf{x} - \mathbf{x}') + i\omega_i (t - t')} \\ &\xrightarrow{\text{continuum}} \int \frac{d^3k}{(2\pi)^3} \frac{1}{2\omega_{\mathbf{k}}} \langle n_{\mathbf{k}} \rangle e^{-i\mathbf{k}\cdot\boldsymbol{\Delta}\mathbf{x} + i\omega_{\mathbf{k}}\delta t} \\ &\xrightarrow{\text{non-rel}} \frac{m^2 e^{im\delta t}}{2} \int \frac{d^3v}{(2\pi)^3} \langle n_{\mathbf{v}} \rangle e^{-im\mathbf{v}\cdot\boldsymbol{\Delta}\mathbf{x} + \frac{i}{2} m v^2 \delta t} \end{aligned} \tag{A4}$$

Here we defined $\boldsymbol{\Delta}\mathbf{x} \equiv \mathbf{x} - \mathbf{x}'$, $\delta t = t - t'$. To find the normalisation of the field ϕ_0, we can compute the its energy density

$$\begin{aligned} \rho_\phi &= \frac{\langle (\dot{\phi})^2 + (\nabla\phi)^2 + m^2\phi^2 \rangle}{2} \simeq m^4 \int \frac{d^3v}{(2\pi)^3} \langle n_{\mathbf{v}} \rangle \\ &\simeq \frac{1}{2} m^2 \phi_0^2 \int d^3v \frac{2\langle n_{\mathbf{v}} \rangle}{(2\pi)^3} \frac{m^2}{\phi_0^2} \equiv \frac{1}{2} m^2 \phi_0^2 \int d^3v f(\mathbf{v}) \end{aligned} \tag{A5}$$

where we traded $\langle n_{\mathbf{v}} \rangle$ with the normalized velocity distribution $f(\mathbf{v})$ via

$$\langle n_{\mathbf{v}} \rangle \approx \frac{\phi_0^2}{2m^2} (2\pi)^3 f(\mathbf{v}) \ . \tag{A6}$$

Therefore, (A4) can be rewritten as

$$\langle\hat{\phi}^-(\mathbf{x},t)\hat{\phi}^+(\mathbf{x}',t')\rangle \approx \frac{\phi_0^2}{4}e^{im\delta t}\int d^3v f(\mathbf{v})e^{-im\mathbf{v}\cdot\mathbf{\Delta x}+\frac{i}{2}mv^2\delta t}. \tag{A7}$$

Assuming for simplicity that the dark matter velocity follows a Gaussian distribution

$$f(\mathbf{v}) = \frac{1}{\pi^{3/2}v_0^3}e^{-(\mathbf{v}+\mathbf{v}_\odot)^2/v_0^2}, \tag{A8}$$

we can compute the first order degree of coherence for the dark matter field:

$$\begin{aligned} &g^{(1)}(\mathbf{x},t;\mathbf{x}',t') \\ &\equiv\frac{\langle\hat{\phi}^-(\mathbf{x},t)\hat{\phi}^+(\mathbf{x}',t')\rangle}{\sqrt{\langle\hat{\phi}^-(\mathbf{x},t)\hat{\phi}^+(\mathbf{x},t)\rangle\langle\hat{\phi}^-(\mathbf{x}',t')\hat{\phi}^+(\mathbf{x}',t')\rangle}} \\ &=e^{im\delta t}\int\frac{d^3v}{\pi^{3/2}v_0^3}e^{-\frac{(\mathbf{v}+\mathbf{v}_\odot)^2}{v_0^2}-im\mathbf{v}\cdot\mathbf{\Delta x}+i\frac{mv^2}{2}\delta t} \\ &=e^{im\delta t-i\frac{\xi\left(\frac{v_\odot^2}{v_0^2}-\zeta^2\right)-m\mathbf{v}_\odot\cdot\mathbf{\Delta x}}{1+\xi^2}-i\frac{3}{2}\tan^{-1}\xi}\frac{e^{-\frac{\xi^2\frac{v_\odot^2}{v_0^2}+\zeta^2}{1+\xi^2}}}{(1+\xi^2)^{3/4}} \end{aligned} \tag{A9}$$

where

$$\xi\equiv\frac{1}{2}mv_0^2(t-t'),\ \zeta\equiv\frac{1}{2}mv_0|\mathbf{x}-\mathbf{x}'|. \tag{A10}$$

For $v_\odot\sim v_0$, the norm of $g^{(1)}|_{\mathbf{x}=\mathbf{x}'}$ falls to e^{-1} when $\xi\sim 1$. Thus $\tau_a\equiv\frac{2}{mv_0^2}$ is the coherence time for axion dark matter field. To get coherence length, consider

$$g^{(1)}|_{t=t'} = e^{-\zeta^2}e^{imv_\odot\cdot(\mathbf{x}-\mathbf{x}')} \tag{A11}$$

Therefore, $\frac{2}{mv_0}$ can be identified as the axion field coherence length $\lambda_{\rm dB}$.

2. Signal Power in a Cavity

$\langle\hat{\phi}^-(\mathbf{x}_1,t_1)\hat{\phi}^+(\mathbf{x}_2,t_2)\rangle$ directly controls the outcome of a haloscope experiment, since the power spectral density, defined as $S_\phi(\omega)\equiv\frac{1}{T}\langle\tilde{\phi}(\mathbf{x}_1,\omega)\tilde{\phi}^*(\mathbf{x}_2,\omega)\rangle$, can be written as

$$\begin{aligned} S_\phi(\omega) &= \frac{\phi_0^2}{4T}\int dt_1dt_2e^{-i\omega(t_1-t_2)}\left(g^{(1)}(\mathbf{x}_1,t_1;\mathbf{x}_2,t_2)+h.c.\right) \\ &\approx\frac{\phi_0^2}{4}\frac{\sin^2\left(\frac{(\omega-m)T}{2}\right)}{\left(\frac{(\omega-m)}{2}\right)^2T}e^{-\frac{|\mathbf{x}_1-\mathbf{x}_2|^2}{\lambda_{\rm dB}^2}}+(\omega\to-\omega) \\ &\xrightarrow{T\to\infty}\frac{\phi_0^2}{2}\pi(\delta(\omega-m)+\delta(\omega+m))e^{-\frac{|\mathbf{x}_1-\mathbf{x}_2|^2}{\lambda_{\rm dB}^2}} \end{aligned} \tag{A12}$$

where we kept the leading order terms in both the oscillatory and non-oscillatory pieces of $g^{(1)}$ only.

Recall that to get the dark matter signal field in a cavity based experiment, one needs to solve [84]

$$\begin{aligned} &\sum_n\left(\omega^2-\omega_n^2-i\frac{\omega\omega_n}{Q_n}\right)\mathbf{E}_n(\mathbf{x})\tilde{e}_n(\omega) \\ &=\int dte^{-i\omega t}g_{a\gamma}\partial_t(\mathbf{B}_0\dot{\phi}(\mathbf{x},t)) = -\omega^2g_{a\gamma}\mathbf{B}_0\tilde{\phi}(\mathbf{x},\omega). \end{aligned} \tag{A13}$$

Letting the signal field be $\mathbf{E}_1$ and writing $\mathbf{B}_0=B_0\hat{n}$, we have

$$\sqrt{\int_V|\mathbf{E}_1|^2}\tilde{e}_1(\omega) = -\frac{g_{a\gamma}B_0\omega^2}{\omega^2-\omega_1^2-i\frac{\omega\omega_1}{Q_1}}\frac{\int_V\mathbf{E}_1^*\cdot\hat{n}\tilde{\phi}(\omega)}{\sqrt{\int_V|\mathbf{E}_1|^2}}. \tag{A14}$$

To read out the signal, we necessarily introduce additional losses in addition to the intrinsic loss. For now, let $Q_1^{-1}\to Q_{\rm eff}^{-1}=Q_0^{-1}+Q_{\rm e}^{-1}$, where Q_0 and $Q_{\rm e}$ are the intrinsic and extrinsic quality factors respectively. Now the signal power after readout is $P_{\rm sig}=\frac{\omega_1}{Q_{\rm e}}\int_V|\mathbf{E}_1|^2\langle e_1(t)e_1(t)\rangle$. Using $\langle\tilde{\phi}(\mathbf{x}_1,\omega)\tilde{\phi}^*(\mathbf{x}_2,\omega')\rangle = S_\phi(\omega)2\pi\delta(\omega-\omega')$, and $Q_{\rm e}=Q_0/\beta$, we find

$$\begin{aligned} P_{\rm sig} =&\frac{\omega_1g_{a\gamma}^2B_0^2\beta}{Q_0}\int\frac{d\omega}{2\pi}\frac{\omega^4}{(\omega^2-\omega_1^2)^2+\left(\frac{\omega\omega_1}{Q_0}(1+\beta)\right)^2} \\ &\times\frac{\int_V\int_{V'}\mathbf{E}_1(\mathbf{x}')\cdot\hat{n}\mathbf{E}_1^*(\mathbf{x})\cdot\hat{n}S_\phi(\omega)}{\int_V\mathbf{E}_1^*\cdot\mathbf{E}_1} \end{aligned} \tag{A15}$$

For a homogeneous and monochromatic axion field $\frac{\sqrt{2\rho}}{m^2}\cos(mt)$, $S_\phi=\frac{\pi\rho}{m^2}(\delta(m-\omega)+\delta(m+\omega))$, and the above expression signal power gives the familiar result. Taking into account DM coherence over the detector by instead using S_ϕ from Eq. (A12), Eq. (A15) yields on resonance $m=\omega_1$

$$\begin{aligned} P_{\rm sig} =&\frac{Q_0g_{a\gamma}^2B_0^2\rho V}{\omega_1}\frac{\beta}{(1+\beta)^2}\times \\ &\times\frac{\int_V\int_{V'}\mathbf{E}_1(\mathbf{x}')\cdot\hat{n}\mathbf{E}_1^*(\mathbf{x})\cdot\hat{n}e^{-\frac{|\mathbf{x}-\mathbf{x}'|^2}{\lambda_{\rm dB}^2}}}{V\int_V\mathbf{E}_1^*\cdot\mathbf{E}_1}. \end{aligned} \tag{A16}$$

This gives precisely Eqs. (5) to (7) for $\beta=1$. Note that if the detector size $\sim|\mathbf{x}-\mathbf{x}'|\ll\lambda_{\rm dB}$, we recover the usual result.

Appendix B: N Resonators of the Same Frequency in Series

In this Appendix we consider N coupled equal-frequency resonators to show that for minimal assumptions about the read-out the signal power fails to scale with N. More general arguments about this are provided in Section IV along with strategies for restoring this extensive scaling.

When all resonators are identical and their resonant frequencies are equal to ω_R, the coupling matrix in Eq. (67) simplifies to

$$M = \begin{bmatrix} i(\omega-\omega_R)+\tau^{-1} & \tau_{\rm e}^{-1}e^{-i\omega n_r d} & \cdots & \tau_{\rm e}^{-1}e^{-i(N-1)\omega n_r d} \\ \tau_{\rm e}^{-1}e^{-i\omega n_r d} & i(\omega-\omega_R)+\tau_2^{-1} & \cdots & \tau_{\rm e}^{-1}e^{-i(N-2)\omega n_r d} \\ \vdots & \vdots & \ddots & \vdots \\ \tau_{\rm e}^{-1}e^{-i(N-1)\omega n_r d} & \tau_{\rm e}^{-1}e^{-i(N-2)\omega n_r d} & \cdots & i(\omega-\omega_R)+\tau^{-1} \end{bmatrix} \tag{B1}$$

where we also assumed the coupling coefficients κ_i to be real for simplicity. Here $\tau^{-1} = \tau_{\rm e}^{-1} + \tau_0^{-1}$. $\tau_0^{-1} = \omega_R/(2Q_0)$ and $\tau_{\rm e}^{-1} = \omega_R/(2Q_{\rm e})$. Fig. 7 shows the signal power from Eqs. (68) and (69). It is clear that the power at the resonance does not grow linearly with the number of resonators. To understand this behavior further, we work out several simplified cases below where solutions can be obtained analytically.

1. Case 1: No Intrinsic Loss

If there is no intrinsic loss, we can take $Q_0^{-1} \to 0$. For a single resonator, Eqs. (68) and (69) on resonance become

$$P_{\text{sig, 1, no loss}}(\omega=\omega_R) = \frac{1}{2}\tau_{\rm e}\bar{J}_{\rm DM}^2|\eta|^2 V \tag{B2}$$

Note that compared to Eq. (75) here we are considering signal collected from one of the two directions in the bus, leading a factor of two difference between these results. For simplicity, let us compare this with a system of 4 resonators in series and consider the response at $\omega = \omega_R$. Letting $b = e^{-i\omega_R n_r d}$, we find

$$\begin{aligned} s_{\rm out} &\propto \begin{pmatrix} 1 \\ b \\ b^2 \\ b^3 \end{pmatrix}^{\rm T} \cdot \begin{bmatrix} \frac{1}{1-b^2} & \frac{b}{b^2-1} & 0 & 0 \\ \frac{b}{b^2-1} & \frac{b^2+1}{1-b^2} & \frac{b}{b^2-1} & 0 \\ 0 & \frac{b}{b^2-1} & \frac{b^2+1}{1-b^2} & \frac{b}{b^2-1} \\ 0 & 0 & \frac{b}{b^2-1} & \frac{1}{1-b^2} \end{bmatrix} \cdot \begin{pmatrix} s_{\rm DM,1} \\ s_{\rm DM,2} \\ s_{\rm DM,3} \\ s_{\rm DM,4} \end{pmatrix} \\ &= \begin{pmatrix} 1 & 0 & 0 & 0 \end{pmatrix} \cdot \begin{pmatrix} s_{\rm DM,1} \\ s_{\rm DM,2} \\ s_{\rm DM,3} \\ s_{\rm DM,4} \end{pmatrix} \end{aligned} \tag{B3}$$

Therefore in the lossless limit the signal power at $\omega = \omega_R$ for $N = 4$ is precisely equal to that of a *single* resonator on resonance, Eq. (B2):

$$P_{\text{sig, 4, no loss}}(\omega=\omega_R) = \frac{1}{2}\tau_{\rm e}\bar{J}_{\rm DM}^2|\eta|^2 V \tag{B4}$$

This result is true for any number of resonators for almost any choice of separation d, *regardless of whether dark matter sources are coherent or not.*

One caveat of the derivation above is that M becomes singular when $b = 1$, or $\omega_R n_r d$ is an integer multiple of 2π, which is exactly the choice that enables a constructive interference in the read-out. This issue can be avoided by keeping τ_0^{-1} and taking $Q_0 \to \infty$ at the end as we show below.

2. Case 2: Coherent Sources

Next, let us consider the response when $\omega = \omega_R$ and the dark matter sources are all coherent, i.e., $s_{{\rm DM},i}$ all have the same phase. This means that the resonator spacing d must be small enough such that $v_0\omega_R d N \ll 1$. Furthermore, let us choose d such that $\omega_R n_r d$ is an integer multiple of 2π in order to address the caveat above. One can show that the contribution to $s_{\rm out}$ from each resonator takes the following form

$$\frac{\beta^{1/2}}{\beta + N^{-1}}\left(\frac{1}{N}, \frac{1}{N}, \frac{1}{N}, \cdots\right), \tag{B5}$$

where β is defined by $Q = Q_0/(1+\beta)$. The total signal power then scales as

$$P_{\text{sig, }N\text{, coherent}}(\omega=\omega_R) = \frac{Q_0}{\omega_R}\frac{N^2\beta}{(1+N\beta)^2}\bar{J}_{\rm DM}^2|\eta|^2 V \tag{B6}$$

The coupling that maximizes the output is $\beta = 1/N$. This corresponds to a "critical coupling" for the entire system for which the signal power becomes:

$$P_{\text{sig, }N\text{, coherent, crit}}(\omega=\omega_R) = \frac{NQ_0}{\omega_R}\bar{J}_{\rm DM}^2|\eta|^2 V. \tag{B7}$$

Compared with Eq. (75) evaluated at critical coupling (which includes an additional factor for 2 for radiation into both directions in the bus), it is clear that the signal power grows linearly with the number of resonators as long as they are within the coherence length of the dark matter.

Using $Q_0 = \beta Q_e$, followed by taking $\beta \to \infty$, Eq. (B6) becomes

$$P_{\text{sig, }N\text{ coherent, no loss}}(\omega=\omega_R) = \frac{1}{2}\tau_{\rm e}\bar{J}_{\rm DM}^2|\eta|^2 V, \tag{B8}$$

in agreement with Eqs. (B2) and (B4), addressing the caveat mentioned in the previous subsection.

3. Case 3: Two Resonators

When $N = 2$ we can write down a short, closed form expression for the signal power as a function of resonator spacing, read out couplings and DM frequency detuning. Letting $\omega = \omega_R(1+\Delta)$, the power is given by

$$P_{\text{sig, 2}}(\Delta,\beta) = \frac{Q_0 \bar{J}_{\text{DM}}^2 |\eta|^2 V}{\omega_R}\beta\times \left[\frac{-\beta\rho\cos(2\alpha+\theta)+\beta^2+\beta+4\Delta^2Q_0^2+1}{-2\beta^2\rho^2\cos(2(\alpha+\theta))+\beta^4+\rho^4} + e^{-\frac{1}{4}(\Delta+1)^2 v_0^2\omega_R^2 d^2}\frac{(1+4\Delta^2Q_0^2)\cos\alpha+4\beta\Delta Q_0\sin\alpha}{-2\beta^2\rho^2\cos(2(\alpha+\theta))+\beta^4+\rho^4}\right] \tag{B9}$$

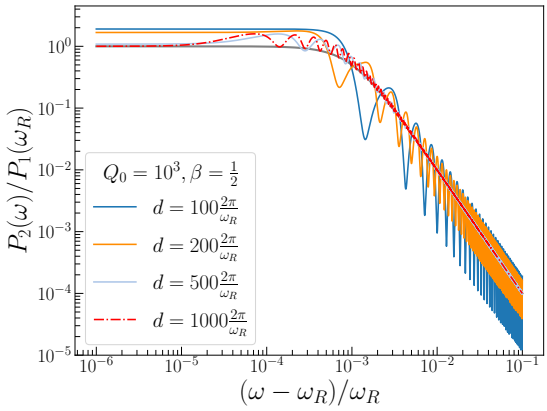

FIG. 11: Signal power from two resonators for different separations d as a function of the relative DM frequency detuning. For comparison, the single resonator power (gray) with $\beta = 1$ is plotted as well. $v_0 = 10^{-3}, n_r = 3.5$

where

$$\alpha(\Delta) = (\Delta+1)n_r\omega_R d \tag{B10a}$$

$$\rho(\Delta,\beta) = \sqrt{(\beta+1)^2+4\Delta^2Q_0^2} \tag{B10b}$$

$$\theta(\Delta,\beta) = \tan^{-1}\left(\frac{2\Delta Q_0}{\beta+1}\right) \tag{B10c}$$

In Fig. 11 we compare the power output from two critically coupled resonators for different separations d. It is clear that as the separation becomes comparable to the dark matter coherence length $\sim \frac{v_0^{-1}}{\pi}\frac{2\pi}{\omega_R}$, the resonance power deteriorates, and increasingly approaches the single resonator power as the separation gets further.

Appendix C: Coupling Optimization

In Section VI A we noted that for a single resonator the signal power is maximized when the intrinsic and external loss rates are equal, $\tau_{\text{i}}^{-1} = \tau_{\text{e}}^{-1}$. In systems with $N > 1$ resonators an analogous optimization can be performed by varying the N resonator-read-out couplings. While we leave a general solution to this problem for future work, in this Appendix we analytically illustrate the behaviour of $N = 2$.

Let us consider two resonators coupled to a receiver. The resonators have slightly different resonant frequencies $\omega_1 = \omega_R$ and $\omega_2 = \omega_R(1+\delta)$ but are otherwise identical, meaning that their intrinsic Q_0 and external $Q_{\text{e}} \equiv Q_0/\beta$ quality factors are the same (so that they both have loaded $Q = Q_0/(1+\beta)$). As a further simplification, let us choose the resonator separation d to be such that $n_r\omega_R d$ is a integer multiple of 2π. This simple setup allows us to study what values of the fractional frequency difference δ and the coupling β would constitute an optimal choice. Assuming that the frequency difference $\delta \sim Q_0^{-1}$, we can write the signal power at the resonant frequencies $\omega_{1,2}$ as

$$\frac{2\bar{J}_{\text{DM}}^2 V|\eta|^2 Q_0}{\omega_R}\sum_{i=0}^{1} f^{(i)}(\beta,\delta)Q_0^{-i}\ . \tag{C1}$$

It turns out that $f^{(0)}$ is the same at $\omega_{1,2}$ and is given by

$$f^{(0)}(\beta,\delta) = \frac{2\beta\left(e^{-\frac{\omega_R^2 d^2 v_0^2}{4}} + 2(\delta Q_0)^2 + 1\right)}{(2\beta+1)^2 + 4(\beta+1)^2(\delta Q_0)^2}\ . \tag{C2}$$

Therefore, one should pick the coupling β such that maximizes the leading contribution to signal power at $\omega_{1,2}$, i.e., $f^{(0)}$. This yields the optimal coupling β^* as a function of frequency difference δ:

$$\beta^*(\delta) = \frac{1}{2}\sqrt{\frac{4(\delta Q_0)^2+1}{(\delta Q_0)^2+1}} \in [\frac{1}{2}, 1]\ , \tag{C3}$$

where the lower limit $\beta = \frac{1}{2}$ occurs at $\delta = 0$, which agrees with a critically coupled system (see Appendix B 2). Figure 12 plots the output power from the two resonator system at the resonant frequencies in leading order of Q_0. If δ is chosen to be a few times Q_0^{-1}, the optimal coupling is approximately 1 for well separated resonators. This implies that each resonator can be treated as independent from each other when they are well separated either in resonance frequencies or in their physical separations.

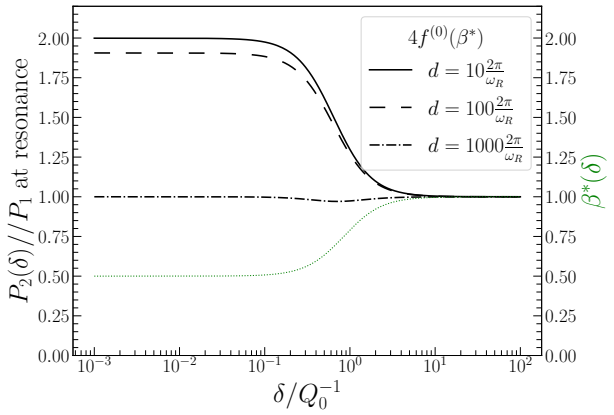

FIG. 12: Leading order power output from two resonator in series at their resonance frequencies as a function of δ. Solid, dashed and dot-dashed lines correspond to three choices of the separation between the resonators. Also shown is the optimal coupling β^* as a function of δ (green dotted). If $\delta \equiv (\omega_2 - \omega_1)/\omega_1$ is chosen to be a few times Q_0^{-1}, the optimal coupling is approximately 1.

Appendix D: Modes of a Cylindrical Fibre Bragg Grating

In this section we provide details of the mode calculation of the 1D-periodic structure discussed in Section III A. In the absence of sources and taking $\varepsilon = \varepsilon(z)$, $\mu_0 = \mu_r = 1, \varepsilon_0 = 1$ the Maxwell equations in Eq. (1) reduce to the following wave equations for harmonic fields

$$(\nabla^2 + \omega^2\varepsilon)\mathbf{E} = -\nabla\left(\frac{\varepsilon' E_z}{\varepsilon}\right) \tag{D1}$$

$$(\nabla^2 + \omega^2\varepsilon)\mathbf{H} = -i\omega\nabla\varepsilon \times \mathbf{E} \tag{D2}$$

We are interested in cylindrically symmetric system. Let $\mathbf{E} \sim \mathbf{E}e^{im\phi}$, $\mathbf{H} \sim \mathbf{H}e^{im\phi}$, the $z-$components of the wave equations are given by

$$\hat{L}_m \begin{pmatrix} E_z \\ H_z \end{pmatrix} = \begin{pmatrix} -(\partial_z \frac{\varepsilon'}{\varepsilon} + \frac{\varepsilon'}{\varepsilon}\partial_z + \omega^2\varepsilon)E_z \\ -\omega^2\varepsilon H_z \end{pmatrix} \tag{D3}$$

where $\hat{L}_m \equiv (\frac{1}{r}\partial_r r \partial_r - \frac{m^2}{r^2} + \partial_z^2)$.

Consider a step index circular waveguide consisting of a core of radius R, and a periodic $\varepsilon(z)$ with periodicity Λ, and a cladding of constant refractive index n_o, and radius much bigger than R. By writing

$$\begin{pmatrix} \sqrt{\varepsilon}E_z \\ H_z \end{pmatrix} = e^{im\phi}\begin{pmatrix} \psi^{\mathrm{TM}}(r,z) \\ \psi^{\mathrm{TE}}(r,z) \end{pmatrix} \tag{D4}$$

we can expand $\psi^\sigma(r,z)$ with $\sigma = \{+ : \mathrm{TM}, - : \mathrm{TE}\}$ in a Bloch series:

$$\psi^\sigma(r,z) = e^{i\beta z}\sum_n \psi_n^\sigma(r)e^{iqnz} \tag{D5}$$

where $q = \frac{2\pi}{\Lambda}$, and $\beta(\omega)$ is the Bloch momentum. Now the wave equations (D3) become

$$\sum_n \left[\partial_r^2 + \frac{1}{r}\partial_r - \frac{m^2}{r^2} - (\beta + qn)^2 + U^\sigma\right]\psi_n^\sigma e^{iqnz} = 0 \tag{D6}$$

where

$$U^{\mathrm{TE}} = \omega^2\varepsilon,\ U^{\mathrm{TM}} = \omega^2\varepsilon - \frac{3}{4}\left(\frac{\varepsilon'}{\varepsilon}\right)^2 + \frac{1}{2}\frac{\varepsilon''}{\varepsilon}. \tag{D7}$$

Expanding U^σ in the Bloch series yields

$$U^\sigma = \omega^2\sum_n U_n^\sigma e^{iqnz} \tag{D8}$$

where $U_n^\sigma = {U_{-n}^\sigma}^*$ due to the reality of U^σ. Substituting this into (D6), we find

$$\begin{aligned}\sum_l \left(\omega^2 U_{n-l}^\sigma - (\beta + qn)^2\delta_{ln}\right)\psi_l^\sigma \\ = -\left(\partial_r^2 + \frac{1}{r}\partial_r - \frac{m^2}{r^2}\right)\psi_n^\sigma.\end{aligned} \tag{D9}$$

For a given polarization σ, this is a set of coupled differential equations for ψ_n^σ. Defining dimensionless variables $\tilde{r} = qr$, $\tilde{\omega} = \omega/q$, matrix $M_{nn'}^\sigma = \tilde{\omega}^2 U_{n-n'}^\sigma - (\frac{\beta}{q} + n)^2\delta_{nn'}$, vector $\Psi^\sigma = \{\psi_n^\sigma\}$, (D9) can be written as

$$\mathbf{M}\cdot\Psi = \mathcal{L}_m(\tilde{r})\Psi\ , -\mathcal{L}_m(\tilde{r}) \equiv \partial_{\tilde{r}}^2 + \frac{1}{\tilde{r}}\partial_{\tilde{r}} - \frac{m^2}{\tilde{r}^2}. \tag{D10}$$

Suppose there exists a matrix $\mathbf{P}$ that diagonalizes $\mathbf{M}$, i.e. $\widetilde{\mathbf{M}} = \mathbf{P}^{-1}\mathbf{M}\mathbf{P}$ is diagonal. Write $\Psi = \mathbf{P}\cdot\tilde{\Psi}$, we get

$$\widetilde{\mathbf{M}}\cdot\tilde{\Psi} = \mathcal{L}_m\tilde{\Psi}. \tag{D11}$$

It is clear that $\widetilde{M}_{nl} = \tilde{\lambda}_l^2\delta_{nl}$, and $\tilde{\Psi}_l = J_m(\tilde{\lambda}_l\tilde{r})$ solve the equations. The problem translates to solving for eigenvalues $\tilde{\lambda}_l^2$ and eigenvectors $\mathbf{c}_l$ of the matrix $\mathbf{M}$. In terms of $\mathbf{c}$'s, $\mathbf{P} = \{\mathbf{c}_1, \mathbf{c}_2, \cdots\}$. Let $\lambda_l \equiv \tilde{\lambda}_l q$, the radial part of the solution can be expressed as

$$\psi_n^\sigma = \begin{cases} \sum_l P_{nl}^\sigma g_l^\sigma \frac{J_m(\lambda_l^\sigma r)}{J_m(\lambda_l^\sigma R)}, & r < R \\ h_n^\sigma \frac{H_m^{(1)}(\alpha_n r)}{H_m^{(1)}(\alpha_n R)}, & r > R \end{cases} \tag{D12}$$

where

$$\alpha_n = \sqrt{\omega^2 n_o^2 - (\beta + qn)^2}\ . \tag{D13}$$

For confined modes, α_n needs to be imaginary. g_l^σ, h_l^σ are to be solved by boundary conditions that require that E_ϕ, E_z, H_ϕ, H_z are continuous at $r = R$.

From the two curl Maxwell equations, we have

$$i\omega H_\phi = \partial_z E_r - \partial_r E_z \tag{D14}$$

$$i\omega H_r = \frac{im}{r}E_z - \partial_z E_\phi \tag{D15}$$

$$-i\omega\varepsilon E_r = \frac{im}{r}H_z - \partial_z H_\phi \tag{D16}$$

$$-i\omega\varepsilon E_\phi = \partial_z H_r - \partial_r H_z \tag{D17}$$

Therefore, after some algebra one obtains

$$(\omega^2\varepsilon+\partial_z^2)E_\phi=\frac{im}{r}(-\frac{1}{2}\frac{\varepsilon'}{\varepsilon^{3/2}}+\frac{\partial_z}{\sqrt{\varepsilon}})(\sqrt{\varepsilon}E_z)-i\omega\partial_r H_z \tag{D18}$$

$$\left(U^{\rm TM}+\partial_z^2\right)\frac{H_\phi}{\sqrt{\varepsilon}}=\frac{im}{r}(-\frac{\varepsilon'}{\varepsilon^{3/2}}+\frac{\partial_z}{\sqrt{\varepsilon}})H_z+i\omega\partial_r(\sqrt{\varepsilon}E_z) \tag{D19}$$

When $m=0$, the TE and TM modes decouple. When $m\neq 0$, the solutions are hybrid modes of TE and TM.

One can write E_ϕ, H_ϕ in the following form:

$$\begin{pmatrix}\frac{H_\phi}{\sqrt{\varepsilon}}\\ E_\phi\end{pmatrix}=e^{iKz}\sum_n e^{iqnz}\begin{pmatrix}\chi_n^+(r)\\ \chi_n^-(r)\end{pmatrix}. \tag{D20}$$

Inside the core, $\varepsilon(z)=\varepsilon(z+\Lambda)$, where the following Bloch series's can be found:

$$\frac{\varepsilon'}{q\varepsilon^{3/2}}=\sum_n B_n e^{iqnz},\ \frac{i}{\sqrt{\varepsilon}}=\sum_n C_n e^{iqnz}. \tag{D21}$$

Define matrix $\mathbf{S}^\sigma$ such that

$$S^\sigma_{nn'}=C_{n-n'}(\frac{\beta}{q}+n')-\gamma^\sigma B_{n-n'} \tag{D22}$$

where $\gamma^\sigma=\frac{1}{2}(1)$ for TM (TE) polarization. Therefore, (D18) and (D19) can be further simplified as

$$\sum_{n'}M^\mp_{nn'}\chi^\mp_{{\rm in}n'}=\frac{im}{\tilde r}\sum_{n'}S^\pm_{nn'}\psi^\pm_{{\rm in}n'}\mp i\tilde\omega\partial_{\tilde r}\psi^\mp_{{\rm in}n} \tag{D23}$$

$$\frac{\alpha_n^2}{q^2}\chi^\mp_{{\rm out}n}=\frac{im}{\tilde r n_o}i(\frac{\beta}{q}+n)\psi^\pm_{{\rm out}n}\mp i\tilde\omega\partial_{\tilde r}\psi^\mp_{{\rm out}n} \tag{D24}$$

Now we are ready to write the boundary conditions. Let matrices $D_{nl}\equiv\frac{i(\beta/q+n)}{(\tilde\omega^2 n_o^2-(\frac{\beta}{q}+n)^2)n_o}\delta_{nl}$, $\mathcal{J}^\sigma_{nl}\equiv\frac{J'_m(\lambda_n^\sigma R)}{J_m(\lambda_n^\sigma R)}\delta_{nl}, \mathcal{H}_{nl}\equiv\frac{1}{\tilde\omega^2 n_o^2-(\frac{\beta}{q}+n)^2}\frac{H'_m(\alpha_n R)}{H_m(\alpha_n R)}\delta_{nl}$, where $'=\partial_{\tilde r}$. The boundary conditions require that

$$\mathbf{P}^\pm\cdot\mathbf{g}^\pm=\mathbf{h}^\pm \tag{D25}$$

$$\pm\frac{m}{\omega R}\left(\mathbf{S}^\pm-\mathbf{M}^\mp\mathbf{D}\right)\cdot\mathbf{h}^\pm=\mathbf{P}^\mp\mathcal{J}^\mp\cdot\mathbf{g}^\mp-\mathbf{M}^\mp\mathcal{H}\cdot\mathbf{h}^\mp \tag{D26}$$

which can be rewritten as $\mathcal{M}\cdot(\mathbf{g}^-\mathbf{g}^+,\mathbf{h}^-,\mathbf{h}^+)^{\rm T}=0$. To have non trivial solutions, it is required that $\det\mathcal{M}=0$. This gives

$$\det\left(\tilde T_{\rm TE}\right)\det\left(\tilde T_{\rm TM}+\left(\frac{m}{\omega R}\right)^2\tilde T_{21}\tilde T_{\rm TE}^{-1}\tilde T_{12}\right)=0 \tag{D27}$$

where

$$\tilde T_\sigma\equiv\mathbf{P}^\sigma\mathcal{J}^\sigma\mathbf{P}^{\sigma-1}-\mathbf{M}^\sigma\mathcal{H}, \tag{D28}$$

$$\tilde T_{12}\equiv\mathbf{S}^+-\mathbf{M}^-\mathbf{D},\ \tilde T_{21}\equiv\mathbf{S}^--\mathbf{M}^+\mathbf{D} \tag{D29}$$

Indeed, when $m=0$, the solutions have either TE or TM polarizations. when $m=1$, the solutions are hybrid modes.

[1] G. Bertone and D. Hooper, Rev. Mod. Phys. **90**, 045002 (2018), arXiv:1605.04909 [astro-ph.CO].
[2] L. F. Abbott and P. Sikivie, Phys. Lett. B **120**, 133 (1983).
[3] M. Dine and W. Fischler, Phys. Lett. B **120**, 137 (1983).
[4] J. Preskill, M. B. Wise, and F. Wilczek, Phys. Lett. B **120**, 127 (1983).
[5] P. Arias, D. Cadamuro, M. Goodsell, J. Jaeckel, J. Redondo, and A. Ringwald, JCAP **06**, 013 (2012), arXiv:1201.5902 [hep-ph].
[6] P. Svrcek and E. Witten, Journal of High Energy Physics **2006**, 051 (2006).
[7] S. A. Abel, M. D. Goodsell, J. Jaeckel, V. V. Khoze, and A. Ringwald, JHEP **07**, 124 (2008), arXiv:0803.1449 [hep-ph].
[8] A. E. Nelson and J. Scholtz, Phys. Rev. D **84**, 103501 (2011), arXiv:1105.2812 [hep-ph].
[9] R. Essig *et al.*, in *Snowmass 2021* (2022) arXiv:2203.08297 [hep-ph].
[10] D. S. Akerib *et al.*, in *Snowmass 2021* (2022) arXiv:2203.08084 [hep-ex].
[11] P. Sikivie, Phys. Rev. Lett. **51**, 1415 (1983), [Erratum: Phys.Rev.Lett. 52, 695 (1984)].
[12] C. Bartram, T. Braine, E. Burns, R. Cervantes, N. Crisosto, N. Du, H. Korandla, G. Leum, P. Mohapatra, T. Nitta, L. J. Rosenberg, G. Rybka, J. Yang, J. Clarke, I. Siddiqi, A. Agrawal, A. V. Dixit, M. H. Awida, A. S. Chou, M. Hollister, S. Knirck, A. Sonnenschein, W. Wester, J. R. Gleason, A. T. Hipp, S. Jois, P. Sikivie, N. S. Sullivan, D. B. Tanner, E. Lentz, R. Khatiwada, G. Carosi, N. Robertson, N. Woollett, L. D. Duffy, C. Boutan, M. Jones, B. H. LaRoque, N. S. Oblath, M. S. Taubman, E. J. Daw, M. G. Perry, J. H. Buckley, C. Gaikwad, J. Hoffman, K. W. Murch, M. Goryachev, B. T. McAllister, A. Quiskamp, C. Thomson, and M. E. Tobar (ADMX Collaboration), Phys. Rev. Lett. **127**, 261803 (2021).
[13] K. M. Backes *et al.* (HAYSTAC), Nature **590**, 238 (2021), arXiv:2008.01853 [quant-ph].
[14] A. J. Brady, C. Gao, R. Harnik, Z. Liu, Z. Zhang, and Q. Zhuang, PRX Quantum **3**, 030333 (2022).
[15] A. V. Dixit, S. Chakram, K. He, A. Agrawal, R. K.

Naik, D. I. Schuster, and A. Chou, Phys. Rev. Lett. **126**, 141302 (2021).
[16] S. Posen, M. Checchin, O. S. Melnychuk, T. Ring, I. Gonin, and T. Khabiboulline, Phys. Rev. Applied **20**, 034004 (2023), arXiv:2201.10733 [physics.acc-ph].
[17] R. Di Vora *et al.*, Phys. Rev. Applied **17**, 054013 (2022), arXiv:2201.04223 [physics.ins-det].
[18] G. Marconato *et al.*, JACoW **SRF2023**, 96 (2023).
[19] D. Antypas *et al.*, (2022), arXiv:2203.14915 [hep-ex].
[20] S. Chaudhuri, P. W. Graham, K. Irwin, J. Mardon, S. Rajendran, and Y. Zhao, Phys. Rev. D **92**, 075012 (2015), arXiv:1411.7382 [hep-ph].
[21] Y. Kahn, B. R. Safdi, and J. Thaler, Phys. Rev. Lett. **117**, 141801 (2016), arXiv:1602.01086 [hep-ph].
[22] A. Berlin *et al.*, (2022), arXiv:2203.12714 [hep-ph].
[23] B. Giaccone *et al.*, (2022), arXiv:2207.11346 [hep-ex].
[24] J. Liu *et al.* (BREAD), Phys. Rev. Lett. **128**, 131801 (2022), arXiv:2111.12103 [physics.ins-det].
[25] S. Beurthey *et al.*, (2020), arXiv:2003.10894 [physics.ins-det].
[26] M. Baryakhtar, J. Huang, and R. Lasenby, Phys. Rev. D **98**, 035006 (2018), arXiv:1803.11455 [hep-ph].
[27] J. Chiles *et al.*, (2021), arXiv:2110.01582 [hep-ex].
[28] R. Cervantes *et al.*, Phys. Rev. D **106**, 102002 (2022), arXiv:2204.09475 [hep-ex].
[29] A. J. Millar *et al.* (ALPHA), Phys. Rev. D **107**, 055013 (2023), arXiv:2210.00017 [hep-ph].
[30] A. Álvarez Melcón *et al.*, JHEP **07**, 084 (2020), arXiv:2002.07639 [hep-ex].
[31] L. Barak *et al.* (SENSEI), Phys. Rev. Lett. **125**, 171802 (2020), arXiv:2004.11378 [astro-ph.CO].
[32] A. Chou *et al.* (2023) arXiv:2311.01930 [hep-ex].
[33] J. W. Foster, N. L. Rodd, and B. R. Safdi, Phys. Rev. D **97**, 123006 (2018), arXiv:1711.10489 [astro-ph.CO].
[34] P. F. de Salas and A. Widmark, Rept. Prog. Phys. **84**, 104901 (2021), arXiv:2012.11477 [astro-ph.GA].
[35] N. W. Evans, C. A. J. O'Hare, and C. McCabe, Phys. Rev. D **99**, 023012 (2019), arXiv:1810.11468 [astro-ph.GA].
[36] C. Wang, X. Xiong, N. Andrade, V. Venkataraman, X.-F. Ren, G.-C. Guo, and M. Lončar, Opt. Express **25**, 6963 (2017).
[37] J. Lee, B. Zhen, S.-L. Chua, W. Qiu, J. D. Joannopoulos, M. Soljačić, and O. Shapira, Phys. Rev. Lett. **109**, 067401 (2012).
[38] J. Li and N. Engheta, Phys. Rev. B **74**, 115125 (2006).
[39] E. N. Bulgakov and A. F. Sadreev, Phys. Rev. A **96**, 013841 (2017).
[40] S. Kim, K.-H. Kim, and J. F. Cahoon, Phys. Rev. Lett. **122**, 187402 (2019).
[41] X. Gao, B. Zhen, M. Soljacic, H. Chen, and C. W. Hsu, ACS Photonics **6**, 2996 (2019).
[42] M. Sidorenko, O. Sergaeva, Z. Sadrieva, C. Roques-Carmes, P. Muraev, D. Maksimov, and A. Bogdanov, Phys. Rev. Appl. **15**, 034041 (2021).
[43] A. Armaroli, A. Morand, P. Benech, G. Bellanca, and S. Trillo, J. Opt. Soc. Am. A **25**, 667 (2008).
[44] D. Zhu, L. Shao, M. Yu, R. Cheng, B. Desiatov, C. J. Xin, Y. Hu, J. Holzgrafe, S. Ghosh, A. Shams-Ansari, E. Puma, N. Sinclair, C. Reimer, M. Zhang, and M. Lončar, Adv. Opt. Photon. **13**, 242 (2021).
[45] J. Flueckiger, S. Schmidt, V. Donzella, A. Sherwali, D. M. Ratner, L. Chrostowski, and K. C. Cheung, Opt. Express **24**, 15672 (2016).
[46] H. Li, L. Wu, Y. Jin, and A. Wu, IEEE Photonics Journal **15**, 1 (2023).
[47] C. W. Hsu, B. Zhen, A. D. Stone, J. D. Joannopoulos, and M. Soljačić, Nature Reviews Materials **1**, 1 (2016).
[48] S. Fan and J. D. Joannopoulos, Phys. Rev. B **65**, 235112 (2002).
[49] J. Jin, X. Yin, L. Ni, M. Soljačić, B. Zhen, and C. Peng, Nature **574**, 501 (2019).
[50] M. Lončar, T. Doll, J. Vučković, and A. Scherer, Journal of lightwave technology **18**, 1402 (2000).
[51] T. Inui, Y. Tanabe, and Y. Y. Onodera, *Group theory and its applications in physics*, 2nd ed., Springer series in solid-state sciences (Springer-Verlag, New York, 1996).
[52] S. G. Johnson and J. D. Joannopoulos, Optics express **8**, 173 (2001).
[53] R. Lasenby, Phys. Rev. D **103**, 075007 (2021), arXiv:1912.11467 [hep-ph].
[54] J. Sun, E. Timurdogan, A. Yaacobi, E. S. Hosseini, and M. R. Watts, Nature **493**, 195 (2013).
[55] S. Kim, D. A. Westly, B. J. Roxworthy, Q. Li, A. Yulaev, K. Srinivasan, and V. A. Aksyuk, Light: Science & Applications **7**, 72 (2018).
[56] M. DeLisio and R. York, IEEE Transactions on Microwave Theory and Techniques **50**, 929 (2002).
[57] P. McManamon, T. Dorschner, D. Corkum, L. Friedman, D. Hobbs, M. Holz, S. Liberman, H. Nguyen, D. Resler, R. Sharp, and E. Watson, Proceedings of the IEEE **84**, 268 (1996).
[58] A. Figotin and I. Vitebskiy, Laser & Photonics Reviews **5**, 201 (2011).
[59] T. Baba, Nature photonics **2**, 465 (2008).
[60] C. Manolatou, M. Khan, S. Fan, P. Villeneuve, H. Haus, and J. Joannopoulos, IEEE Journal of Quantum Electronics **35**, 1322 (1999).
[61] J. Heebner, R. Grover, and T. Ibrahim, *Optical Microresonators: Theory, Fabrication, and Applications*, Optical Sciences, 138 (Springer, 2008).
[62] D. Rabus and C. Sada, *Integrated Ring Resonators: A Compendium*, Springer Series in Optical Sciences (Springer International Publishing, 2020).
[63] B. Desiatov, A. Shams-Ansari, M. Zhang, C. Wang, and M. Lončar, Optica **6**, 380 (2019).
[64] H. Lin, Z. Luo, T. Gu, L. C. Kimerling, K. Wada, A. Agarwal, and J. Hu, Nanophotonics **7**, 393 (2018).
[65] R. Armand, M. Perestjuk, A. Della Torre, M. Sinobad, A. Mitchell, A. Boes, J.-M. Hartmann, J.-M. Fedeli, V. Reboud, P. Brianceau, A. De Rossi, S. Combrié, C. Monat, and C. Grillet, APL Photonics **8**, 071301 (2023).
[66] D. A. Kozak, N. F. Tyndall, M. W. Pruessner, W. S. Rabinovich, and T. H. Stievater, Opt. Express **29**, 15443 (2021).
[67] C. O'Hare, "cajohare/axionlimits: Axionlimits," `https://cajohare.github.io/AxionLimits/` (2020).
[68] A. Caputo, A. J. Millar, C. A. J. O'Hare, and E. Vitagliano, Phys. Rev. D **104**, 095029 (2021), arXiv:2105.04565 [hep-ph].
[69] P. Xu, D. Bond, I. Dixon, and H. Bai, IEEE Transactions on Applied Superconductivity **33**, 1 (2023).
[70] C. L. Hendrickson, J. P. Quinn, N. K. Kaiser, D. F. Smith, G. T. Blakney, T. Chen, A. G. Marshall, C. R. Weisbrod, and S. C. Beu, Journal of the American Society for Mass Spectrometry **26**, 1626 (2015), pMID:

26091892.
[71] K. Thulborn, E. Lui, J. Guntin, S. Jamil, Z. Sun, T. C. Claiborne, and I. C. Atkinson, NMR in Biomedicine **29**, 137 (2016).
[72] N. Boulant, L. Quettier, G. Aubert, A. Amadon, J. Belorgey, C. Berriaud, C. Bonnelye, P. Bredy, E. Chazel, G. Dilasser, O. Dubois, E. Giacomini, G. Gilgrass, V. Gras, Q. Guihard, V. Jannot, F. P. Juster, H. Lannou, F. Leprêtre, C. Lerman, C. Le Ster, M. Luong, F. Mauconduit, F. Molinié, F. Nunio, L. Scola, A. Sinanna, R. Touzery, P. Védrine, A. Vignaud, and the Iseult Consortium, Magnetic Resonance Materials in Physics, Biology and Medicine **36**, 175 (2023).
[73] T. F. Budinger and M. D. Bird, NeuroImage **168**, 509 (2018), neuroimaging with Ultra-high Field MRI: Present and Future.
[74] Y. Hochberg, B. V. Lehmann, I. Charaev, J. Chiles, M. Colangelo, S. W. Nam, and K. K. Berggren, Phys. Rev. D **106**, 112005 (2022), arXiv:2110.01586 [hep-ph].
[75] P. Adari *et al.* (SENSEI), (2023), arXiv:2312.13342 [astro-ph.CO].
[76] V. Anastassopoulos *et al.* (CAST), Nature Phys. **13**, 584 (2017), arXiv:1705.02290 [hep-ex].
[77] A. Ayala, I. Domínguez, M. Giannotti, A. Mirizzi, and O. Straniero, Phys. Rev. Lett. **113**, 191302 (2014), arXiv:1406.6053 [astro-ph.SR].
[78] M. J. Dolan, F. J. Hiskens, and R. R. Volkas, JCAP **10**, 096 (2022), arXiv:2207.03102 [hep-ph].
[79] E. Todarello, M. Regis, J. Reynoso-Cordova, M. Taoso, D. Vaz, J. Brinchmann, M. Steinmetz, and S. L. Zoutendijke, (2023), arXiv:2307.07403 [astro-ph.CO].
[80] D. Grin, G. Covone, J.-P. Kneib, M. Kamionkowski, A. Blain, and E. Jullo, Phys. Rev. D **75**, 105018 (2007), arXiv:astro-ph/0611502.
[81] R. Janish and E. Pinetti, (2023), arXiv:2310.15395 [hep-ph].
[82] H. An, M. Pospelov, J. Pradler, and A. Ritz, Phys. Rev. D **102**, 115022 (2020), arXiv:2006.13929 [hep-ph].
[83] R. Loudon, *The Quantum Theory of Light*, 2nd ed. (Clarendon Press, Oxford, 1983).
[84] C. Gao and R. Harnik, JHEP **07**, 053 (2021), arXiv:2011.01350 [hep-ph].